



Raytheon

SURFACE ALBEDO

VISIBLE/INFRARED IMAGER/RADIOMETER SUITE

ALGORITHM THEORETICAL BASIS DOCUMENT

Version 4: May 2001

Shawn W. Miller
Peter Vogt

Shunlin Liang (University of Maryland), Phase I Science Team Member

RAYTHEON SYSTEMS COMPANY
Information Technology and Scientific Services
4400 Forbes Boulevard
Lanham, MD 20706

SBRS Document #: Y2398

EDR: SURFACE ALBEDO

Doc No: Y2398

Version: 4

Revision: 0

	Function	Name	Signature	Date
Prepared by	EDR Developer	S. MILLER		
Approved by	Relevant IPT Lead	S. MILLER		
Approved by	Chief Scientist	S. MILLER		
Released by	Program Manager	P. KEALY		

TABLE OF CONTENTS

	<u>Page</u>
LIST OF FIGURES	iii
LIST OF TABLES	v
LIST OF TABLES	v
GLOSSARY OF ACRONYMS	vi
GLOSSARY OF ACRONYMS	vi
ABSTRACT ix	
1.0 INTRODUCTION	1
1.1 PURPOSE	1
1.2 SCOPE	2
1.3 VIIRS DOCUMENTS	2
1.4 REVISIONS	3
2.0 EXPERIMENT OVERVIEW	5
2.1 OBJECTIVES OF SURFACE ALBEDO RETRIEVAL	5
2.2 INSTRUMENT CHARACTERISTICS	6
2.3 RETRIEVAL STRATEGY	10
3.0 ALGORITHM DESCRIPTION	12
3.1 PROCESSING OUTLINE	12
3.2 ALGORITHM INPUT	13
3.2.1 VIIRS Data	14
3.2.2. Non-VIIRS Data	14
3.3. THEORETICAL DESCRIPTION OF ALGORITHM	14
3.3.1. Physics of the Problem	14
3.3.2. Mathematical Description of Algorithm	14
3.3.2.1 Dark Surfaces—Adapted MODIS Approach (SASA1)	15
3.3.2.2 Bright Surfaces—Neural Network Approach (SASA2)	18
3.4 ALGORITHM SENSITIVITY STUDIES	24
3.4.1 EDR Requirements	24
3.4.2 Performance Metrics	25
3.4.3 Individual Error Sources	27
3.4.3.1 Phase I Sensor Error Evaluations	27

3.4.3.2	Atmospheric Correction Errors	30
3.4.3.3	BRDF Effects	30
3.4.3.4	Narrow to Broadband Conversion	31
3.4.3.5	TOA Reflectance Errors.....	32
3.4.3.6	Neural Network Intrinsic Errors	42
3.5.	PRACTICAL CONSIDERATIONS.....	45
3.5.1.	Numerical Computation Considerations.....	45
3.5.2.	Programming and Procedural Considerations.....	46
3.5.3.	Configuration of Retrievals.....	46
3.5.4.	Quality Assessment and Diagnostics	46
3.5.5.	Exception Handling.....	47
3.6.	VALIDATION.....	47
4.0	ASSUMPTIONS AND LIMITATIONS	52
4.1	ASSUMPTIONS.....	52
4.2	LIMITATIONS.....	52
5.0	REFERENCES	54

LIST OF FIGURES

	<u>Page</u>
Figure 1. Summary of VIIRS design concepts and heritage.	7
Figure 2. VIIRS detector footprint aggregation scheme for building "pixels."	8
Figure 3. Benefits of VIIRS aggregation scheme in reducing pixel growth at edge of scan.	8
Figure 4. VIIRS spectral bands, visible and near infrared.	9
Figure 5. VIIRS spectral bands, short wave infrared.	9
Figure 6. Software processing architecture for the Surface Albedo EDR.....	12
Figure 7. Software processing architecture for the Gridded Surface Albedo IP.....	13
Figure 8. Spectral decoupling of atmospheric and surface properties for derivation of broadband albedo.....	19
Figure 9. Graph of the sigmoid function, $y=1/(1+e^{-x})$	20
Figure 10. Surface Albedo EDR neural network architecture.....	22
Figure 11. Angular binning to address BRDF variations in the Phase I Surface Albedo EDR algorithm. New baseline replaces this strategy with direct use of three angles as additional inputs to the neural network.	24
Figure 12. Narrow to broadband albedo conversion errors from Phase I evaluation of a Lambertian-based linear regression algorithm, using the combinations of channels listed in Table 9 for four different backgrounds.....	32
Figure 13. TOA reflectance errors at 412 nm, for nadir and edge of scan, at solar zenith of 30 degrees (top) and 70 degrees (bottom), using both specified and predicted sensor performance as input.	34
Figure 14. TOA reflectance errors at 445 nm, for nadir and edge of scan, at solar zenith of 30 degrees (top) and 70 degrees (bottom), using both specified and predicted sensor performance as input.	35
Figure 15. TOA reflectance errors at 488 nm, for nadir and edge of scan, at solar zenith of 30 degrees (top) and 70 degrees (bottom), using both specified and predicted sensor performance as input.	36
Figure 16. TOA reflectance errors at 555 nm, for nadir and edge of scan, at solar zenith of 30 degrees (top) and 70 degrees (bottom), using both specified and predicted sensor performance as input.	37
Figure 17. TOA reflectance errors at 645 nm, for nadir and edge of scan, at solar zenith of 30 degrees (top) and 70 degrees (bottom), using both specified and predicted sensor performance as input.	38

Figure 18. TOA reflectance errors at 865 nm, for nadir and edge of scan, at solar zenith of 30 degrees (top) and 70 degrees (bottom), using both specified and predicted sensor performance as input.....	39
Figure 19. TOA reflectance errors at 1240 nm, for nadir and edge of scan, at solar zenith of 30 degrees (top) and 70 degrees (bottom), using both specified and predicted sensor performance as input.....	40
Figure 20. TOA reflectance errors at 1610 nm, for nadir and edge of scan, at solar zenith of 30 degrees (top) and 70 degrees (bottom), using both specified and predicted sensor performance as input.....	41
Figure 21. TOA reflectance errors at 2250 nm, for nadir and edge of scan, at solar zenith of 30 degrees (top) and 70 degrees (bottom), using both specified and predicted sensor performance as input.....	42
Figure 22. Albedo accuracy performance, spec and predicted, at edge of scan for a solar zenith of 30 degrees. Note negligible difference between spec and predicted sensor performance for calibration, assuming the algorithm is trained post-launch with real VIIRS data.	44
Figure 23. Albedo uncertainty performance, spec and predicted, at nadir for a solar zenith of 70 degrees. Nadir uncertainty requirement (fine product) is 0.03 threshold.	45

LIST OF TABLES

	<u>Page</u>
Table 1. Parameter definitions relevant to the Surface Albedo EDR.....	1
Table 2. The nine VIIRS spectral bands used in the baseline Surface Albedo algorithm.....	10
Table 3. Inputs required by the Surface Albedo EDR baseline algorithm.....	13
Table 4. VIIRS SRD prescribed requirements for the Surface Albedo EDR (TBR = to be reviewed, TBD = to be determined).....	24
Table 5. Indexed combinations of channels considered for conversion from narrow to broadband albedo for Phase I evaluation of the Lambertian-based regression algorithm.....	31
Table 6. Summary of dimensions for the Phase I TOA Reflectance and SASA2 stick modeling data set.....	33
Table 7. Phase II results for SASA2 over snow, at the edge of the VIIRS scan.....	43
Table 8. Ground based instruments for the AVP.....	49
Table 9. Airborne instruments for the AVP.....	50
Table 10. Satellite measurements to compare with VIIRS for the AVP.....	50
Table 11. Possible testbeds for the AVP.....	50

GLOSSARY OF ACRONYMS

ACE	Aerosol Characterization Experiment
ADD	Algorithm Data Definition
AERONET	Aerosol Robotic Network
AirMISR	Airborne Multi-angle Imaging Spectroradiometer
AOT	Aerosol Optical Thickness
APAR	Absorbed Photosynthetically Active Radiation
ARA	Albedo Retrieval Algorithm
ARM CART	Atmospheric Radiation Measurement, Cloud and Radiation Testbed
ARQI	Aerosol Retrieval Quality Indicator
ASAS	Advanced Solid-state Array Spectroradiometer
ATBD	Algorithm Theoretical Basis Document
ATS	Applications Technological Satellite
ATSR	Along-Track Scanning Radiometer
AVHRR	Advanced Very High Resolution Radiometer
AVIRIS	Airborne Visible and Infrared Imaging Spectrometer
AVP	Albedo Validation Plan
BBA	Broadband Albedo
BOREAS	Boreal Ecosystem/Atmosphere Study
BRDF	Bidirectional Reflectance Distribution Function
BRF	Bidirectional Reflectance Factor
CP	Calibration Panel
EDR	Environmental Data Record
EOPACE	Electro-optic Propagation Assessment in Coastal Environment
EOS	Earth Observing System
FAPAR	Fraction of APAR
GCM	General Circulation Model
GPS	Global Positioning System
HAPEX	Hydrological-Atmospheric Pilot Experiment
HCS	Horizontal Cell Size
ICD	Interface Control Document
ID	Identification Number of Input/Output Data for Processing Modules

IFOV	Instantaneous Field of View
IGBP	International Geosphere-Biosphere Project
IP	Intermediate Product
IPO	Integrated Program Office
ISIS	Integrated Surface Irradiance Study
LADF	Leaf Angle Distribution Function
LAI	Leaf Area Index
LCC	Land Cover Class
LQF	Land Quality Flag(s)
LUT	Look-up table
MAS	MODIS Airborne Simulator
MFRSR	Multifilter Rotating Shadowband Radiometer
MISR	Multangle Imaging Spectroradiometer
MODIS	Moderate Resolution Imaging Spectroradiometer
MODTRAN	Moderate Resolution Transmission Model
MTF	Modulation Transfer Function
NASA	National Aeronautics and Space Administration
NBAR	Nadir BRDF-Adjusted Reflectance
NDVI	Normalized Difference Vegetation Index
NIR	Near Infrared
NOAA	National Oceanic and Atmosphere Administration
NPP	Net Primary Production OR NPOESS Preparatory Project
NPOESS	National Polar-orbiting Operational Environmental Satellite System
OAA	Ocean Albedo Algorithm
OTTER	Oregon Transect Ecosystem Research
PAR	Photosynthetically Active Radiation
PARABOLA	Portable Apparatus for Rapid Acquisition of Bidirectional Observations of Land and Atmosphere
POLDER	Polarization and Directionality of the Earth's Reflectances
PSF	Point Spread Function
RDQI	Radiometric Data Quality Indicator
RDR	Raw Data Record
RMS	Root Mean Square

RT	Radiative Transfer
SASA1	Surface Albedo Sub-Algorithm 1 (Adapted MODIS Approach)
SASA2	Surface Albedo Sub-Algorithm 2 (Neural Network)
SCAR-B	Smoke, Clouds, and Radiation (Brazil)
SDR	Sensor Data Record
SeaWiFS	Sea-viewing, Wide-Field-of-View Sensor
SNR	Signal-to-Noise Ratio
SRD	Sensor Requirements Document
SVQI	Subregion Variability Quality Indicator
SWIR	Short Wave Infrared
TARFOX	Tropospheric Aerosol Radiative Forcing Observational Experiment
TBD	To Be Determined
TM	Thematic Mapper (Landsat)
TOA	Top-of-Atmosphere
TOC	Top-of-Canopy
VI	Vegetation Index
VVI	VIIRS Vegetation Index
VIIRS	Visible/Infrared Imager/Radiometer Suite

ABSTRACT

This document describes the algorithm for retrieving the Surface Albedo Environmental Data Record (EDR) as part of the requirements for the Visible/Infrared Imager/Radiometer Suite (VIIRS), the primary visible and infrared sensor to be flown onboard the platforms of the National Polar-orbiting Operational Environmental Satellite System (NPOESS) and the NPOESS Preparatory Project (NPP). Surface Albedo is defined in the VIIRS Sensor Requirements Document (SRD) to be a ratio of broadband fluxes at the Earth's surface, extending spectrally from 0.3 to 4.0 μm . Also required in the most recent version of the SRD is the intermediate derivation of directional surface reflectances; that process is described in a separate document (VIIRS Surface Reflectance ATBD, Y2411). The SRD requirements for the Surface Albedo are challenging for even moderately bright surfaces, particularly with respect to precision. This EDR has therefore undergone extensive trade analyses during Phase I and Phase II of the VIIRS algorithm development effort. The end result of these analyses is a two-tiered strategy: a Moderate Resolution Imaging Spectroradiometer (MODIS)-like approach for dark surfaces such as vegetation and water, combined with a neural network approach for bright surfaces such as desert and snow. The adapted MODIS approach will be used to produce daily, gridded black-sky albedo, white sky albedo, and associated weights and coefficients from the computations at 1-km resolution across the globe, using a running window of 16-days worth of gridded surface reflectances from the Gridded Daily Surface Reflectance Intermediate Product (IP). The gridded black sky and white sky albedo values will be interpolated and used to derive pixel-level broadband surface albedo for dark surfaces during real-time operational processing. The neural net is run entirely in real time, using current top of atmosphere (TOA) reflectances at the pixel level. Recent validations of the MODIS algorithm performance instill significant confidence that the EDR requirements can be met for dark surfaces. Preliminary analyses of the neural network approach suggest the requirements are also achievable for snow and desert, however verification of these results requires more rigorous and realistic treatment of surface bidirectional effects.

1.0 INTRODUCTION

1.1 PURPOSE

This Algorithm Theoretical Basis Document (ATBD) explains the physical and mathematical background for an algorithm to derive the Surface Albedo Environmental Data Record (EDR) as a part of the requirements for the Visible/Infrared Imager/Radiometer Suite (VIIRS), the primary visible and infrared instrument to be flown onboard the platforms of the National Polar-orbiting Operational Environmental Satellite System (NPOESS). The algorithm is also targeted toward the requirements for the NPOESS Preparatory Project (NPP), an endeavor by the National Aeronautics and Space Administration (NASA) to continue the heritage of the MODerate-resolution Imaging Spectroradiometer (MODIS) and provide a bridge to the operational implementation of VIIRS. In addition, this document provides an overview of the required input data, a physical and mathematical description of the algorithm and its predicted performance, assumptions and limitations, and a sensitivity study of the described algorithm. The single EDR described in this document is one of over two dozen EDRs within the NPOESS/VIIRS system. Table 1 summarizes some definitions and naming conventions for parameters relevant to discussions of surface albedo. These terms will be used throughout this document.

Table 1. Parameter definitions relevant to the Surface Albedo EDR.

Symbol	Definition/Comments	Units
θ	Solar zenith angle	rad
ϑ	View zenith angle	rad
ϕ	Relative azimuth angle	rad
λ	Wavelength	μm
Δ	Waveband Δ of width $\Delta\lambda$	None
$\tau(\lambda)$	Atmospheric optical depth	None
$S(\theta, \tau(\lambda))$	Fraction of diffuse skylight, assumed isotropic	None
$D(\theta, \lambda, \tau(\lambda))$	Bottom of atmosphere downwelling radiative flux	$\text{Wm}^{-2}\mu\text{m}^{-1}$
$U(\theta, \lambda, \tau(\lambda))$	Bottom of atmosphere upwelling radiative flux	$\text{Wm}^{-2}\mu\text{m}^{-1}$
D_{BB}	Broadband bottom of atmosphere downwelling flux	Wm^{-2}
U_{BB}	Broadband bottom of atmosphere upwelling flux	Wm^{-2}
$\rho(\theta, \vartheta, \phi, \Delta)$	Observed surface reflectance (atmospherically corrected)	None
$\rho_{TOA}(\theta, \vartheta, \phi, \Delta)$	Observed top of atmosphere reflectance	None
$R(\theta, \vartheta, \phi, \Delta)$	Bidirectional reflectance distribution function (BRDF)	None
$K_k(\theta, \vartheta, \phi)$	BRDF model kernel k	None
$h_k(\theta)$	Integral of BRDF model kernel k over ϑ and ϕ	None
H_k	Integral of $h_k(\theta)$ over θ	None
$f_k(\Delta)$	BRDF kernel model parameter k in waveband Δ	None
$a_{bs}(\theta, \lambda)$	Spectral black-sky albedo	None
$a_{ws}(\lambda)$	Spectral white-sky albedo	None
$a(\theta, \lambda)$	Spectral albedo	None
$A(\theta)$	Broadband albedo	None

1.2 SCOPE

This document covers the theoretical basis for the derivation of the Surface Albedo EDR and the Gridded Surface Albedo Intermediate Product (IP). Focus and emphasis are placed on the two sub-algorithms baselined for operational retrievals. Surface reflectances, now required as an intermediate derived product for the Surface Albedo EDR, are retrieved by a separate algorithm, which is described in the Surface Reflectance ATBD [Y2411].

The purpose and scope of this document are described in this section. Section 2 gives an overview of the EDR retrieval objectives and operations concept. Section 3 describes the baseline algorithm, its input data requirements, the theoretical background, sensitivity analyses, error budgeting, and some practical considerations. Section 4 lists the assumptions and limitations associated with the algorithm presented here, and Section 5 presents the references cited.

1.3 VIIRS DOCUMENTS

This document contains references to other VIIRS documents that are given in italicized brackets. Most of the references are indexed to the Raytheon Santa Barbara Remote Sensing (SBRS) Y-number database for officially released documents. The VIIRS documents thus cited are listed below:

Y2387 VIIRS Soil Moisture ATBD

Y2388 VIIRS Aerosol Optical Thickness and Particle Size ATBD

Y2390 VIIRS Suspended Matter ATBD

Y2393 VIIRS Cloud Effective Particle Size and Cloud Optical Thickness ATBD

Y2400 VIIRS Vegetation Index ATBD

Y2401 VIIRS Snow Cover/Depth ATBD

Y2402 VIIRS Surface Type ATBD

Y2411 VIIRS Surface Reflectance ATBD

Y2412 VIIRS Cloud Mask ATBD

Y2468 VIIRS Operations Concept Document

Y2469 VIIRS Context Level Software Architecture

Y2470 VIIRS Interface Control Document (ICD)

Y2474 VIIRS Land Module Level Software Architecture

Y2483 VIIRS Land Module Level Detailed Design

Y2499 VIIRS Surface Albedo Unit Level Detailed Design

Y3236 VIIRS Software Integration and Test Plan

Y3237 VIIRS Algorithm Verification and Validation Plan

Y3251 VIIRS Precipitable Water ATBD

Y3252 VIIRS Active Fires ATBD

Y3257 VIIRS Computer Resources Requirements Document

Y3261 VIIRS Radiometric Calibration ATBD

Y3270 VIIRS System Verification and Validation Plan

Y3279 VIIRS Land Module Level Interface Control Document

Y6635 VIIRS Algorithm Software Development Plan

Y6661 VIIRS Algorithm Software Maturity Assessment

Y7040 VIIRS Algorithm/Data Processing Technical Report

Y7051 VIIRS Earth Gridding ATBD

SS154650 VIIRS System Specification

PS154650 VIIRS Sensor Specification

PS154640 VIIRS Algorithm Specification

1.4 REVISIONS

This is Version 4 of the Surface Albedo ATBD. It is dated May 2001. The original version of this document was dated July 1998. Version 1 was dated September 1998. Version 2 was dated June 1999. Version 3 was dated May 2000. The author would like to thank Peter Vogt for extensive work on previous versions of this document. Shunlin Liang provided a great deal of insight and guidance for Phase I trades, and Crystal Schaaf has already provided significant advice with regard to merging the MODIS albedo heritage into the VIIRS operational baseline.

2.0 EXPERIMENT OVERVIEW

2.1 OBJECTIVES OF SURFACE ALBEDO RETRIEVAL

Surface albedo is one of the most important parameters characterizing the earth's radiative regime and its impact on biospheric and climatic processes (Dickinson, 1995; Lofgren, 1995; Henderson-Sellers *et al.*, 1993). Albedo defines the lower boundary layer for atmospheric radiative transfer and details the total shortwave energy input into the biosphere and thus is a key component of the surface energy budget. The spatial and temporal distribution of surface properties captured by the bi-directional reflectance distribution function (BRDF) and albedo features reflect a variety of natural and human influences on the surface that are of interest to global climate research.

Albedo specifies the fraction of incident solar radiation that is reflected at the Earth's surface. It is a critical parameter for accurate climate and energy balance studies (Dickinson, 1983; Mintz, 1984; Henderson-Sellers and Pitman, 1992; Running, 1990, 1994; Saunders, 1990; Sellers *et al.*, 1996). Historically, land cover maps (Matthews, 1983; Wilson and Henderson-Sellers, 1985) have been used to derive the albedo. Satellite data offer a unique opportunity to create maps of land cover or any other parameter of interest (LAI, FAPAR, NPP, etc.) to the scientific community and climate researchers. They permit the global observation and quantification of the temporal and spatial distribution and variability of different land cover types. The albedo of a given land cover type can change quickly through processes such as deforestation, soil moisture change, agricultural expansion, harvesting, flooding, and snow melting. These changes result in a modification of the hydrological and thermal state of the surface on local to regional scale. On a long-term scale, they might result in severe drought periods as for the Sahel-region (Charney *et al.*, 1977) or reductions in precipitation (Nemani *et al.*, 1996).

Within the past hundred years, strong growth in human population and industrialization have led to a significant increase in biomass burning. As a result, a noticeable augmentation of the atmospheric trace gas CO₂ has been recorded for many years (Graedel and Crutzen, 1994). The thermal radiation emitted by the earth is absorbed and re-radiated by CO₂. This process induces a heating of the atmosphere via the greenhouse effect. This heating directly interacts with the albedo via snow/ice melting or desertification. Thus, a precise assessment of the albedo is crucial for the evaluation of climate change. In order to assess the effect of anthropogenic changes to the environment, complex models have been designed. Ecosystem studies and general circulation models (GCMs) critically depend on the surface albedo in order to forecast the impact of natural and anthropogenic changes to the environment (Sellers *et al.*, 1994; Lean and Rowntree, 1993; Garratt, 1993; Chase *et al.*, 1996; Culf *et al.*, 1995). They forecast future developments and permit the appropriate economic, social and political reactions. These reactions might include changes in land use, provisions to reduce greenhouse gas emissions, and the redirection of scientific research aims in order to better understand the chemical and biogeophysical interaction between climate change and the anthroposphere.

In Earth resources remote sensing, spectral radiances that are reflected from the surface and received by the sensor are a function of many components. These include the continuously varying incident solar irradiance (e.g., geometry and spectral distribution), atmospheric conditions (e.g., water vapor and aerosols), meteorological conditions (e.g., cloud cover, temperature, wind, dew), reflectance properties of the surface (e.g., spatial, spectral, and

biophysical conditions), and sensor viewing conditions (geometry, time of observation). The spectral bidirectional reflectance factor (BRF) describes these components while the spatial distribution of the BRFs is provided by the BRDF. A surface displaying identical BRFs for all directions is called isotropic or Lambertian. The assumption of a Lambertian surface leads to very simple algorithmic approaches for albedo retrieval, but research in the past 15 years has conclusively established that the Earth's surface is non-Lambertian (anisotropic). Kimes and Sellers (1985) demonstrated the importance of considering BRDF effects. They showed that when BRDF effects are neglected, errors in spectral albedo of up to 40 percent could occur. Off-nadir viewing data is no longer treated as "noisy data" with respect to nadir observation but as a potential new information source to determine:

- Vegetation-specific characteristics (e.g., LAI, LADF, crown size, ground cover fraction; Pinty and Verstraete, 1991; Kimes and Sellers, 1985).
- Land cover classification (Leroy *et al.*, 1997).
- Water leaving radiances, and thus marine phytoplankton concentration, in areas exposed to sun glint at nadir observation (Gordon *et al.*, 1983).
- Atmospheric phase-function (Vermote, 1996; Martonchik and Diner, 1992).

Partially in response to these issues, different sensors have been built with the capability to increase our understanding of BRDF effects. New sensors, such as the Moderate Resolution Imaging Spectroradiometer (MODIS), the Multi-angle Imaging SpectroRadiometer (MISR), the Along Track Scanning Radiometer (ATSR), and POLarization and Directionality of the Earth's Reflectances (POLDER), offer more spectral channels and directions of observation than had been previously available. As a result, the quality of albedo retrievals is expected to improve. The VIIRS algorithm will leverage this algorithm technological progress to provide an operational albedo product that will build and improve upon an already burgeoning heritage.

2.2 INSTRUMENT CHARACTERISTICS

The VIIRS instrument will now be briefly described to clarify the context of the descriptions of the Surface Albedo EDR presented in this document. VIIRS can be pictured as a convergence of three existing sensors, two of which have seen extensive operational use at this writing.

The Operational Linescan System (OLS) is the operational visible/infrared scanner for the Department of Defense (DoD). Its unique strengths are controlled growth in spatial resolution through rotation of the ground instantaneous field of view (GIFOV) and the existence of a low-level light sensor (LLLS) capable of detecting visible radiation at night. OLS has primarily served as a data source for manual analysis of imagery. The Advanced Very High Resolution Radiometer (AVHRR) is the operational visible/infrared sensor flown on the National Oceanic and Atmospheric Administration (NOAA) Television Infrared Observation Satellite (TIROS-N) series of satellites (Planet, 1988). Its unique strengths are low operational and production cost and the presence of five spectral channels that can be used in a wide number of combinations to produce operational and research products. In December 1999, NASA launched the EOS morning satellite, *Terra*, which includes MODIS. This sensor possesses an unprecedented array of thirty-two spectral bands at resolutions ranging from 250 m to 1 km at nadir, allowing for currently unparalleled accuracy in a wide range of satellite-based environmental measurements.

VIIRS will reside on a platform of the NPOESS series of satellites. It is intended to be the product of a convergence between DoD, NOAA and NASA in the form of a single visible/infrared sensor capable of satisfying the needs of all three communities, as well as the research community beyond. As such, VIIRS will require three key attributes: high spatial resolution with controlled growth off nadir, minimal production and operational cost, and a large number of spectral bands to satisfy the requirements for generating accurate operational and scientific products.

Figure 1 illustrates the design concept for VIIRS, designed and built by Raytheon Santa Barbara Remote Sensing (SBRS). At its heart is a rotating telescope scanning mechanism that minimizes the effects of solar impingement and scattered light. VIIRS is essentially a combination of SeaWiFS fore-optics and an all-reflective modification of MODIS/THEMIS aft-optics. Calibration is performed onboard using a solar diffuser for short wavelengths and a blackbody source and deep space view for thermal wavelengths. A solar diffuser stability monitor (SDSM) is also included to track the performance of the solar diffuser. The nominal altitude for NPOESS will be 833 km. The VIIRS scan will therefore extend to 56 degrees on either side of nadir.

The VIIRS SRD places explicit requirements on spatial resolution for the Imagery EDR. Specifically, the horizontal spatial resolution (HSR) of bands used to meet threshold Imagery EDR requirements must be no greater than 400 m at nadir and 800 m at the edge of the scan. This led to the development of a unique scanning approach which optimizes both spatial resolution and signal to noise ratio (SNR) across the scan. The concept is summarized in Figure 2 for the imagery bands; the nested lower resolution radiometric bands follow the same paradigm at exactly twice the size. The VIIRS detectors are rectangular, with the smaller dimension along the scan. At nadir, three detector footprints are aggregated to form a single VIIRS "pixel." Moving along the scan away from nadir, the detector footprints become larger both along track and along scan, due to geometric effects and the curvature of the Earth. The effects are much larger along scan. At around 32 degrees in scan angle, the aggregation scheme is changed from 3x1 to 2x1. A similar switch from 2x1 to 1x1 aggregation occurs at 48 degrees. The VIIRS scan consequently exhibits a pixel growth factor of only 2 both along track and along scan, compared with a growth factor of 6 along scan which would be realized without the use of the aggregation scheme. Figure 3 illustrates the benefits of the aggregation scheme for spatial resolution.

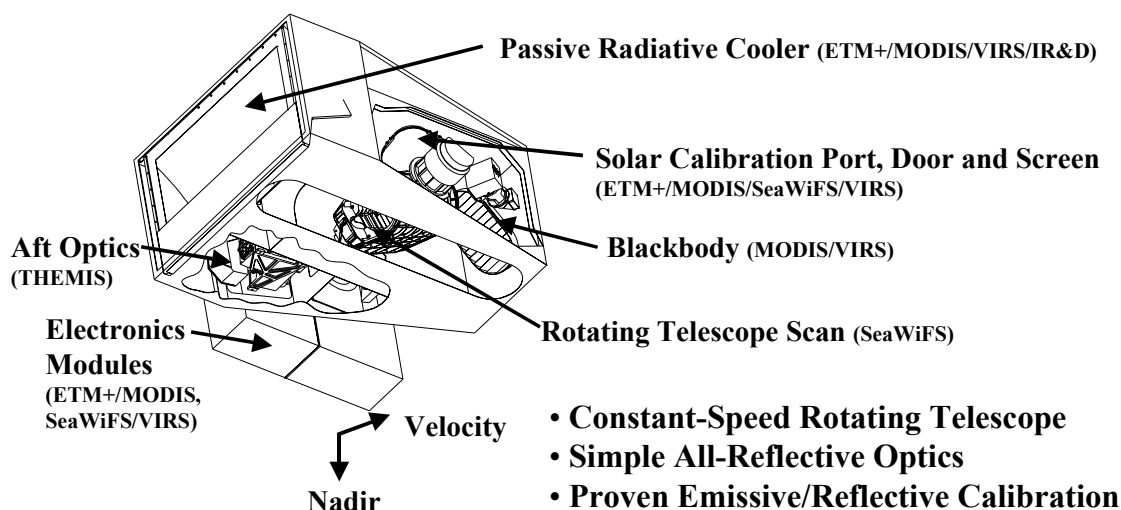


Figure 1. Summary of VIIRS design concepts and heritage.

Fine-Resolution Bands

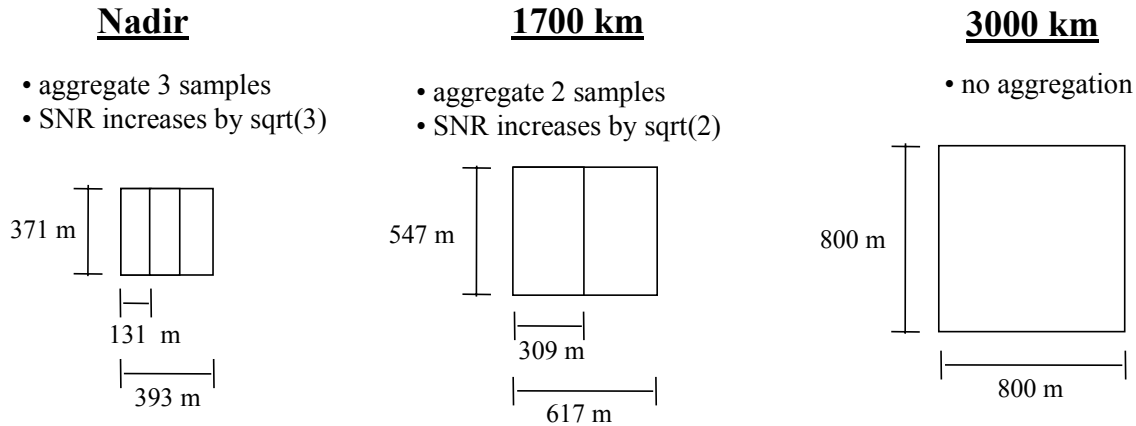


Figure 2. VIIRS detector footprint aggregation scheme for building "pixels."

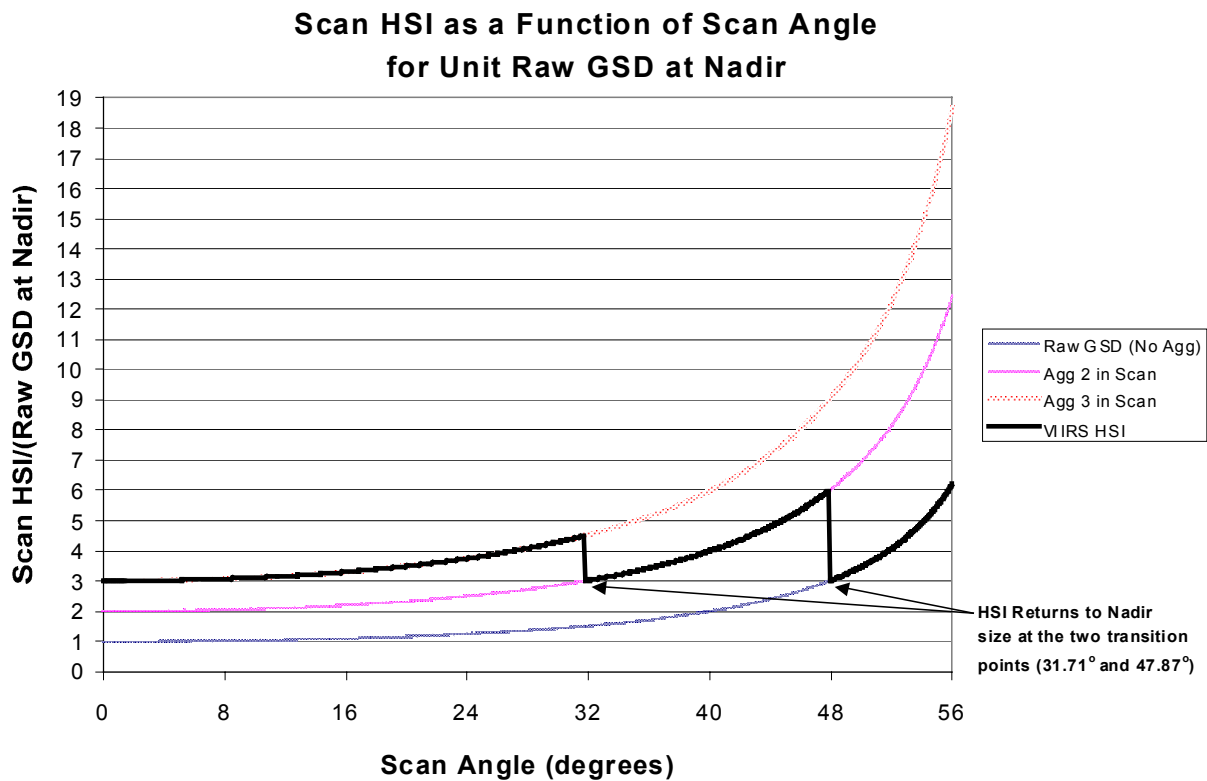


Figure 3. Benefits of VIIRS aggregation scheme in reducing pixel growth at edge of scan.

This scanning approach is extremely beneficial for the retrieval of land products such as Surface Albedo. The increasing importance of land cover change detection makes high spatial resolution in surface albedo and its input reflectances much more important, and signal to noise ratio (SNR) becomes a secondary issue (this latter point will be verified later in this document). The

positioning of the VIIRS spectral bands in the range required by the Surface Albedo EDR is summarized in Figure 4 and Figure 5. Details of the radiometric, spectral, and spatial performance of these bands can be found in the VIIRS Sensor Specification [PS154650].

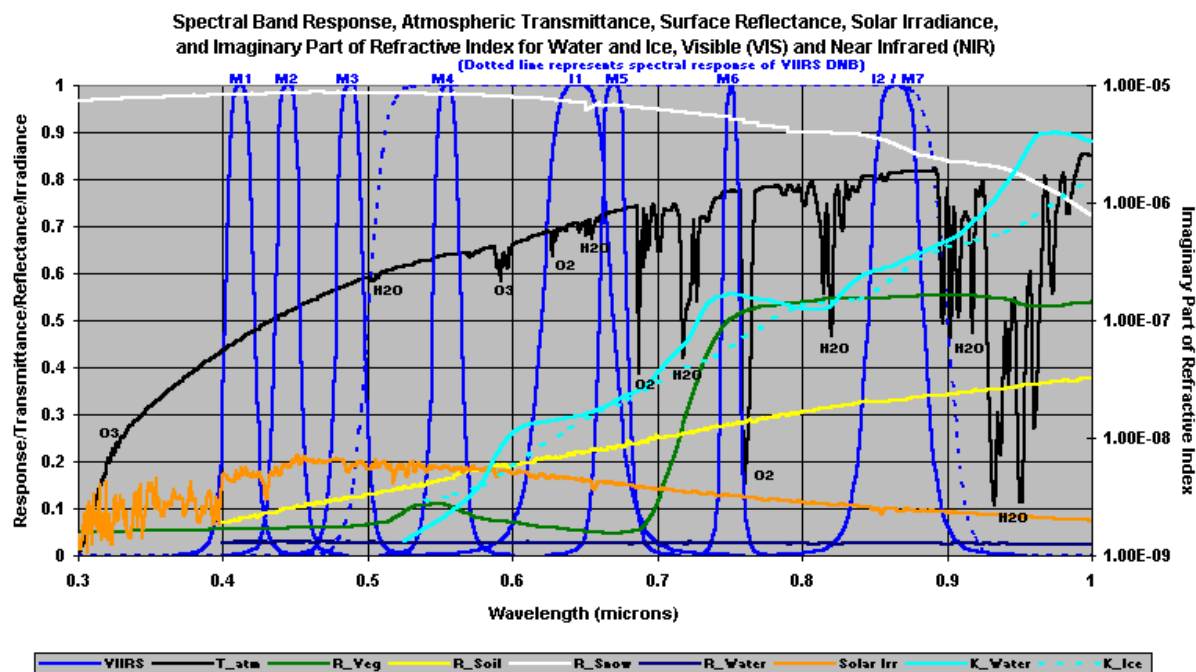


Figure 4. VIIRS spectral bands, visible and near infrared.

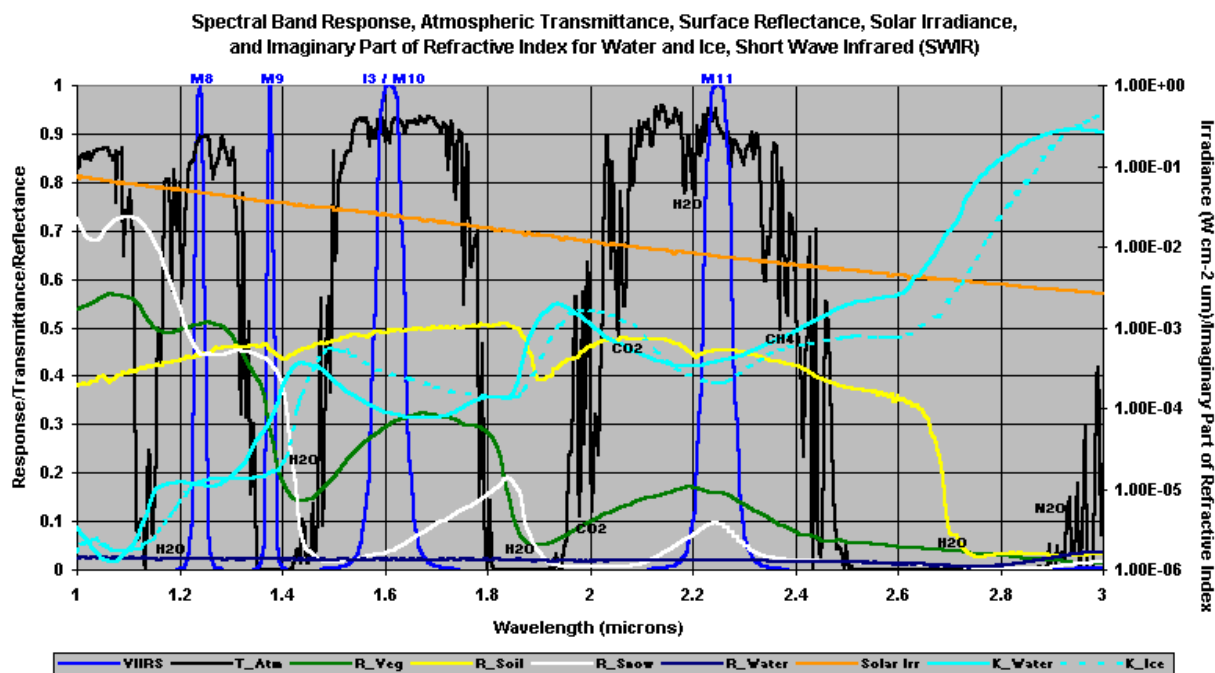


Figure 5. VIIRS spectral bands, short wave infrared.

2.3 RETRIEVAL STRATEGY

The Surface Albedo EDR will be computed for all clear, daytime pixels at the VIIRS moderate resolution (approximately 750 m at nadir). A clear moderate resolution pixel in this context has been flagged either “definitely clear,” “probably clear,” or “probably cloudy” by the VIIRS Cloud Mask. If the pixel is “probably clear” or “probably cloudy,” the retrieval will be flagged in the generalized Land Quality Flag (LQF) output appended to the VIIRS Surface Reflectance Intermediate Product (IP). Retrievals will also be generated for pixels that have been categorized as thin cirrus by the VIIRS Cloud Mask [Y2412]. The strategy for correcting thin cirrus and the limits of applying this correction are discussed in [Y2411]. A daytime pixel is one for which the average solar zenith angle is less than or equal to 85 degrees. Pixels with a solar zenith angle of 70 degrees or higher are flagged in the LQF output. Nine spectral bands from VIIRS are used to generate the Surface Albedo EDR; these are listed in Table 2. Three of these bands are at imagery resolution (375 m at nadir); these bands are aggregated 2x2 to moderate resolution before the albedo is computed. This approach has been taken to improve the spatial sharpness of the data leading into the Surface Albedo EDR at the three wavelengths carrying the bulk of the spectral information from the surface.

Table 2. The nine VIIRS spectral bands used in the baseline Surface Albedo algorithm.

Band Name	Center (microns)	Width (microns)	Nadir Spatial Resolution (m)
M1	.412	.020	750
M2	.445	.018	750
M3	.488	.020	750
M4	.555	.020	750
I1	.645	.050	375
I2	.865	.039	375
M8	1.24	.020	750
I3	1.61	.060	375
M11	2.25	.050	750

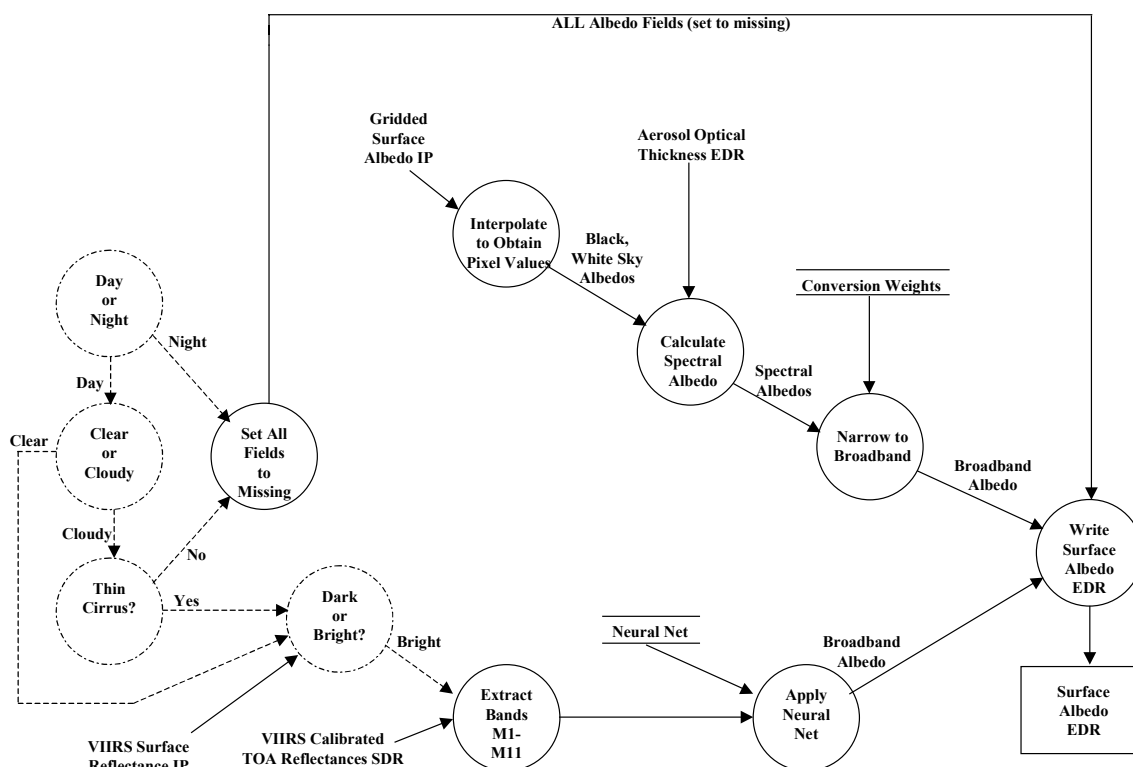
There are two sub-algorithms utilized to produce the Surface Albedo EDR. Surface Albedo Sub-Algorithm 1 (SASA1) is based on the MODIS approach, and is used for all dark surfaces, including most vegetation and water. Surface Albedo Sub-Algorithm 2 (SASA2) is a neural network approach, and it used for all bright surfaces, including snow, desert, and many instances of bare soil. The present strategy is to make these algorithms completely complementary, such that if one is used, the other is not. SASA1 involves the production of the Gridded Surface Albedo IP, which is interpolated to obtain the necessary input for real time processing. As a

result, black sky albedo, white sky albedo, and the associated model weights and coefficients will be available on a global basis independently from the instantaneous retrieval of albedo in VIIRS pixels, should the end user wish to apply the MODIS approach for all surfaces.

3.0 ALGORITHM DESCRIPTION

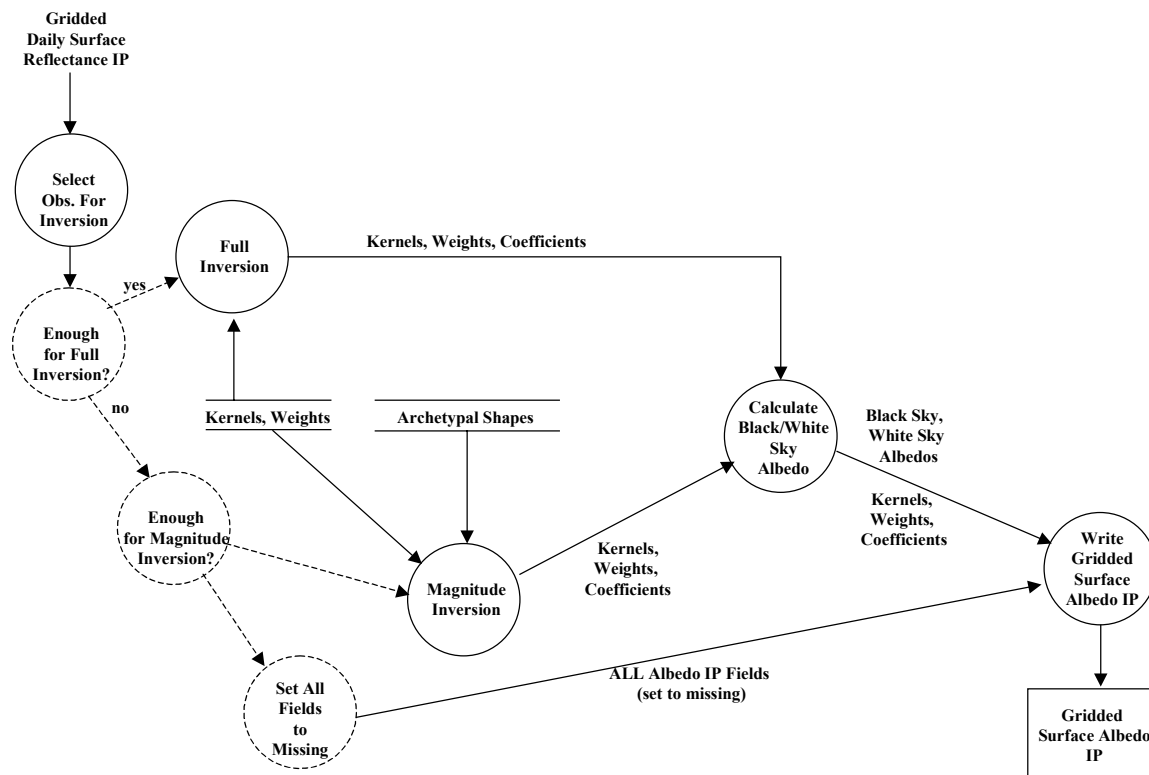
3.1 PROCESSING OUTLINE

Figure 6 illustrates the software architecture for the real-time processing of the Surface Albedo EDR. Once a pixel has qualified as daytime and clear, the VIIRS Surface Reflectance IP facilitates a measure of surface brightness. If the brightness is less than a TBD threshold, SASA1 will be run using the Gridded Surface Albedo IP, the generation of which is shown pictorially in Figure 7. Otherwise, SASA2 will commence using the VIIRS Calibrated TOA Reflectances Sensor Data Record (SDR [Y3261]). The details of SASA1 and SASA2 are presented in Sections 3.3.2.1 and 3.3.2.2, respectively.



6.4 - SURFACE ALBEDO EDR

Figure 6. Software processing architecture for the Surface Albedo EDR.



6.4 - SURFACE ALBEDO EDR (Gridded Surface Albedo IP)

Figure 7. Software processing architecture for the Gridded Surface Albedo IP.

3.2 ALGORITHM INPUT

The required inputs for the Surface Albedo EDR algorithm are listed in Table 3.

Table 3. Inputs required by the Surface Albedo EDR baseline algorithm.

Input Data	Source of Data	Reference
Calibrated TOA Reflectances SDR	Build SDR Module	[Y3261]
Surface Reflectance IP	VIIRS Land Module	[Y2411]
Aerosol Optical Thickness EDR	VIIRS Aerosol Module	[Y2388]
Gridded Daily Surface Reflectance IP	Build SDR Module	[Y7051]
Neural Network Weights for SASA2	Offline Processing	<i>This document</i>
Kernels, Weights for SASA1	Offline Processing	<i>This document</i>
Narrow-to-Broadband Coefficients	Offline Processing	<i>This document</i>

3.2.1 VIIRS Data

To determine whether a surface is dark (use SASA1) or bright (use SASA2), the VIIRS Surface Reflectance IP is required. For dark surfaces, the SASA1 real-time processing requires the VIIRS Aerosol Optical Thickness EDR, precomputed narrow-to-broadband conversion coefficients, and the VIIRS Gridded Surface Albedo IP. This last product is generated offline, once per day, and requires the Gridded Daily Surface Reflectance IP, a 16-day collection of gridded surface reflectances at 1-km resolution globally. Generation of the Gridded Surface Albedo IP also requires a precomputed set of kernels and weights to convert directional surface reflectance observations into black-sky and white-sky albedo estimates. SASA2 only requires precomputed neural network weights and the VIIRS Calibrated TOA Reflectances SDR for real-time processing.

3.2.2. Non-VIIRS Data

The Surface Albedo EDR and Gridded Surface Albedo IP algorithms do not require any data from sources outside the VIIRS system.

3.3. THEORETICAL DESCRIPTION OF ALGORITHM

3.3.1. Physics of the Problem

Albedo is related to surface reflectance through the integration of the Bidirectional Reflectance Distribution Factor (BRDF), which describes the intrinsic anisotropic character of the surface. Specification of the BRDF provides surface reflectance explicitly in terms of its spectral, directional, spatial and temporal characteristics. Both BRDF and albedo are determined by surface structure and optical properties. Typical structural phenomena for vegetation include: the gap distribution between vegetated areas, vegetation height and style, leaf angle distribution function, and the hotspot—a local reflectance maximum caused by the absence of shadows in the retrosolar position. Over ocean, the wind speed roughens the water surface. Over snow, the snow grain size and the contribution of soot have a strong impact on the reflectance field.

The importance of including BRDF features in the interpretation of satellite-derived data has been emphasized by many researchers (Pinty and Verstraete, 1991; Liang and Strahler, 1993; Nilson and Kuusk, 1989; Ross and Marshak, 1989; Jupp and Strahler, 1991; Andrieu *et al.*, 1997; Vogt, 1997). Neglecting BRDF effects can result in serious deviations when calculating the spectral and broadband albedo (Han, 1996; Qi *et al.*, 1995; Schaaf and Strahler, 1993; Lee and Kaufman, 1986).

3.3.2. Mathematical Description of Algorithm

The fundamental definitions of parameters related to Surface Albedo retrievals, summarized in Table 1, are now detailed more extensively, to provide a stronger context for the mathematical descriptions of SASA1 and SASA2. This discussion largely parallels that provided in Lucht *et al.* (2000).

Consider a satellite-based sensor observing the surface at a view zenith angle ϑ . The sun illuminates this surface at a solar zenith angle θ , and ϕ is the relative azimuth angle between the sun and the sensor. A number of important quantities relating to albedo are functions of spectral

wavelength, which will be designated by λ . The sensor observing the surface will integrate over λ to deliver measurements in a spectral waveband Λ .

Intervening between the surface and the sensor is an atmosphere, which has an optical depth $\tau(\lambda)$. In the bands most relevant to albedo retrieval, the majority of this optical depth arises from Rayleigh and aerosol scattering, and the effects of these processes become larger with decreasing λ . Were there no atmosphere present, the only significant radiation propagating from the sun to the surface and back to the sensor is in the form of direct beams. The more aerosols are present in the atmosphere, or the shorter the wavelength λ , the greater the fraction of direct and reflected solar radiation that exists as diffuse, scattered light. The fraction of diffuse skylight, assumed here to be isotropic, is represented by $S(\theta, \tau(\lambda))$. At the bottom of the atmosphere, combined diffuse and direct downwelling radiative flux is $D(\theta, \lambda, \tau(\lambda))$, and the upwelling flux is $U(\theta, \lambda, \tau(\lambda))$.

The surface reflects some portion of the incident solar radiation, a process that can be characterized by the surface reflectance, which is a function of the solar and viewing geometry combined with the properties of the surface itself. We define the atmospherically corrected observed reflectance in a given waveband as $\rho(\theta, \vartheta, \phi, \Lambda)$. This quantity exists within the VIIRS system as the Gridded Daily Surface Reflectance IP. It is a directional reflectance corresponding to one particular combination of solar and viewing geometry. The manner in which geometry alone affects $\rho(\theta, \vartheta, \phi, \Lambda)$ in a given band is characterized by the surface bi-directional reflectance distribution function (BRDF), $R(\theta, \vartheta, \phi, \Lambda)$.

Spectral albedo is defined as the ratio of spectral upwelling radiative flux $U(\theta, \lambda, \tau(\lambda))$ to spectral downwelling radiative flux $D(\theta, \lambda, \tau(\lambda))$ at the surface, and therefore involves integration over the hemisphere represented by the range of possible values for ϑ and ϕ . Broadband albedo, the primary output of the Surface Albedo EDR, is defined as the ratio of broadband fluxes $U_{BB}(\theta, \tau(\lambda))$ and $D_{BB}(\theta, \tau(\lambda))$. Spectral albedo $a(\theta, \Lambda)$ can be considered a combination of two other quantities: the spectral black-sky albedo $a_{bs}(\theta, \Lambda)$ and the spectral white-sky albedo $a_{ws}(\theta, \Lambda)$. The spectral black-sky albedo is defined as the spectral albedo in the absence of a diffuse component, and the spectral white-sky albedo is defined as the spectral albedo in the absence of a direct component, assuming an isotropic diffuse component. Black-sky albedo is therefore a function of the solar zenith angle θ , while white-sky albedo is a constant for a given band Λ . The degree to which each of $a_{bs}(\theta, \Lambda)$ and $a_{ws}(\Lambda)$ contribute to $a(\theta, \Lambda)$ is determined by the fraction of diffuse skylight $S(\theta, \tau(\lambda))$. Conversion from the observed spectral albedo $a(\theta, \Lambda)$ to the observed broadband albedo $A(\theta)$ involves approximating an integration over λ using measurements from several spectral bands Λ .

3.3.2.1 Dark Surfaces—Adapted MODIS Approach (SASA1)

The MODIS heritage algorithm (Wanner *et al.*, 1995;1997; Lucht *et al.*, 2000; Schaaf *et al.*, 2001) has been adapted for retrieval of the VIIRS Surface Albedo EDR over dark surfaces, where confidence in aerosol retrieval leading into surface reflectance is high. The MODIS algorithm relies on the accumulation of registered, multi-date, multi-band, cloud-free, atmospherically-corrected surface reflectance data and a semiempirical BRDF model to produce periodic, frequently-updated, a priori BRDF shapes. These shapes are then convolved with

subsequent daily surface observations in a magnitude inversion procedure (Strugnell and Lucht, 2001; Strugnell *et al.*, 2001) to produce daily BRDFs, daily albedo values (both spectral and broadband) and daily Nadir BRDF-Adjusted Reflectances (NBAR). The semiempirical kernel-driven BRDF model implemented in the prototype code is known as the RossThickLiSparseReciprocal kernel combination and consists of a linear weighted sum of a volume-scattering kernel (based on single-scattering radiative transfer theory), a surface-scattering kernel (based on geometric optics), and an isotropic constant. These kernels (Roujean *et al.*, 1992; Wanner *et al.*, 1995; and Lucht *et al.*, 2000). are based on parameterizations of physical models developed by Ross (1981) and Li and Strahler (1992) and have been shown to perform well over a wide range of surface types (Privette *et al.*, 1997). The linear nature of these models result in rapid computation and the kernels themselves can be easily updated as new kernels are developed by the scientific community. Semiempirical models in general are used routinely with remotely sensed data from AVHRR (Li *et al.*, 1996; d'Entremont *et al.*, 1999), MISR (Rahman *et al.*, 1993; Martonchik *et al.*, 1998), and Meteosat (Pinty *et al.*, 2000a;b). Kernel-driven models in particular are being used operationally with data from the MODIS (Wanner *et al.*, 1997; Lucht *et al.*, 2000; Schaaf *et al.*, 2001) and POLDER (Leroy *et al.*, 1997; Hauteceur and Leroy, 1998, Bicheron and Leroy, 2000) instruments.

To model the BRDF, one may employ a kernel-based approach:

$$R(\theta, \vartheta, \phi, \Lambda) = \sum_k f_k(\Lambda) K_k(\theta, \vartheta, \phi), \quad (1)$$

where $K_k(\theta, \vartheta, \phi)$ is the BRDF model kernel k , and f_k is the BRDF kernel model parameter k in waveband Λ . For MODIS and VIIRS albedo retrievals, there are three kernels, as discussed above: the volume-scattering kernel k_{vol} ; the surface-scattering kernel k_{geo} ; and an isotropic constant k_{iso} . These kernels are developed a priori as functions of solar and viewing geometry. Their respective weighting coefficients $f_k(\Lambda)$ vary and must be determined at run-time to compute the BRDF $R(\theta, \vartheta, \phi, \Lambda)$. If we have a series of reflectance observations $\rho_i(\theta_i, \vartheta_i, \phi_i, \Lambda)$, we can attempt to fit $R(\theta, \vartheta, \phi, \Lambda)$ to these observations by optimizing $f_k(\Lambda)$. This involves minimization $\partial e^2 / \partial f_k = 0$ of a least-squares error function

$$e^2(\Lambda) = \frac{1}{d} \sum_i \frac{(\rho(\theta_i, \vartheta_i, \phi_i, \Lambda) - R(\theta_i, \vartheta_i, \phi_i, \Lambda))^2}{w_i(\Lambda)}, \quad (2)$$

where $w_i(\Lambda)$ is a weight given to each observation and d are the degrees of freedom, equal to the number of observations minus the number of parameters $f_k(\Lambda)$. Equation (2) leads to analytical solutions for $f_k(\Lambda)$:

$$f_k(\Lambda) = \sum_i \left\{ \frac{\sum_j \frac{\rho(\theta_j, \vartheta_j, \phi_j, \Lambda) K_i(\theta_j, \vartheta_j, \phi_j)}{w_j(\Lambda)}}{\left(\sum_l \frac{K_i(\theta_l, \vartheta_l, \phi_l) K_k(\theta_l, \vartheta_l, \phi_l)}{w_l(\Lambda)} \right)^{-1}} \right\}. \quad (3)$$

The term in brackets is the inversion matrix of a linear system. This inversion allows the computation of $f_k(\Lambda)$ such that $e^2(\Lambda)$ is minimized, allowing an approximation of the BRDF shape so that the individual observations of directional reflectance can be hemispherically integrated into a retrieval of the albedo. If we define the directional-hemispherical (ϑ and ϕ) integral of the BRDF model kernels as

$$h_k(\theta) = \frac{1}{\pi} \int_0^{2\pi} \int_0^{\pi/2} K_k(\theta, \vartheta, \phi) \sin(\vartheta) \cos(\vartheta) d\vartheta d\phi \quad (4)$$

and the bihemispherical integral (θ , ϑ , and ϕ) of the BRDF model kernels as

$$H_k = 2 \int_0^{\pi/2} h_k(\theta) \sin(\theta) \cos(\theta) d\theta, \quad (5)$$

then the black-sky and white-sky albedo are given respectively by

$$a_{bs}(\theta, \Lambda) = \sum_k f_k(\Lambda) h_k(\theta) \quad (6)$$

and

$$a_{ws}(\Lambda) = \sum_k f_k(\Lambda) H_k. \quad (7)$$

The kernel integrals $h_k(\theta)$ and H_k do not depend on the observations; these can be precomputed and stored. Only the weighting coefficients $f_k(\Lambda)$, which determine the relative contributions of volume scattering, surface scattering, and the isotropic constant, need to be retrieved from the observations. Lucht *et al.* (2000) illustrated how the integral $h_k(\theta)$ can be represented by simple polynomial parameterizations of solar zenith angle θ .

$$h_k(\theta) = g_{0k} + g_{1k}\theta^2 + g_{2k}\theta^3, \quad (8)$$

where g_{0k} , g_{1k} , and g_{2k} have been precomputed for each of the three kernels k . The white-sky integral H_k has been precomputed as a constant for each of the three kernels k . Once a series of observations of $\rho(\theta, \vartheta, \phi, \Lambda)$ have been used to invert Equation (3) and solve for the weighting coefficients $f_k(\Lambda)$, the black-sky and white-sky albedo for the present solar zenith angle θ are computed respectively as

$$\begin{aligned} a_{bs}(\theta, \Lambda) = & f_{iso}(\Lambda)(g_{0iso} + g_{1iso}\theta^2 + g_{2iso}\theta^3) \\ & + f_{vol}(\Lambda)(g_{0vol} + g_{1vol}\theta^2 + g_{2vol}\theta^3) \\ & + f_{geo}(\Lambda)(g_{0geo} + g_{1geo}\theta^2 + g_{2geo}\theta^3) \end{aligned} \quad (9)$$

and

$$a_{ws}(\Lambda) = f_{iso}(\Lambda)H_{iso} + f_{vol}(\Lambda)H_{vol} + f_{geo}(\Lambda)H_{geo}. \quad (10)$$

These represent the two extremes in albedo, all-diffuse and all-direct. To compute the actual spectral albedo $a(\theta, \Lambda)$, one can interpolate between $a_{bs}(\theta, \Lambda)$ and $a_{ws}(\Lambda)$ as shown in Lewis and Barnsley (1994):

$$a(\theta, \Lambda) = [1 - S(\theta, \tau(\Lambda))]a_{bs}(\theta, \Lambda) + S(\theta, \tau(\Lambda))a_{ws}(\Lambda), \quad (11)$$

where $S(\theta, \tau(\Lambda))$ is the atmospheric state, primarily a function of aerosol optical thickness τ (neglecting variations in Rayleigh scattering). $S(\theta, \tau(\Lambda))$ can be tabulated based on radiative transfer (RT) modeling and stored for use at the time of albedo retrieval, assuming a measurement of the aerosol optical thickness τ is available.

The final step in computing the Surface Albedo EDR for dark surfaces is the conversion from narrowband spectral albedo $a(\theta, \Lambda)$ to broadband albedo $A(\theta)$. For MODIS, this is done using conversion factors as computed by Liang *et al.* (1999). These spectral weighting factors for inherent albedos are derived from numerous MODTRAN-4 calculations over a range of cover types. The total shortwave albedo (0.3-5.0 μm) as well as the visible portion (0.3-0.7 μm) and NIR/SWIR portion (0.7-5.0 μm) are computed. The underlying assumption is that the use of a "typical" atmospheric state, essentially a characterization of τ , is sufficient to produce robust coefficients regardless of the actual atmospheric state. For VIIRS, further sensitivity studies should be conducted using MODIS data to confirm the validity of this assumption with regard to meeting the system specifications. Also, new coefficients will need to be derived to account for slight changes in spectral and spatial characteristics in the relevant bands, and to calibrate to the required spectral range of 0.3-4.0 μm .

3.2.2.2 Bright Surfaces—Neural Network Approach (SASA2)

The use of SASA1 for albedo retrievals hinges upon one key assumption: the availability of an accurate aerosol optical thickness estimation. If this assumption does not hold, the propagation of the resulting errors through the retrieval of surface reflectance, diffuse skylight fraction, atmospheric state, and the various subsets of albedo itself will endanger the ability of the VIIRS system to meet the specifications for the Surface Albedo EDR. For bright surfaces, such as snow and desert, where the broadband albedo significantly exceeds approximately 0.3, the VIIRS system specification for aerosol optical thickness quality suggests absolute errors in surface reflectance that are too high to allow the meeting of the Surface Albedo EDR requirements. This does not even take into account other factors, such as the computation of diffuse skylight fraction. Consequently, in order to reduce risk for retrieval of Surface Albedo over bright surfaces, we have implemented a neural network solution that works directly from current measurements of TOA reflectance.

A number of earlier studies, such as Chen and Ohring (1984), Pinker (1985), Koepke and Kriebel (1987), and Li and Garand (1984), have linearly related TOA spectral albedo to surface broadband albedo. In the past, however, such methods have been limited in two ways: nonlinearity in the true relationship and the lack of spectral information at global resolution. Until the launch of the Terra spacecraft in late 1999, the only consistent source of visible, near infrared (NIR), and short wave infrared (SWIR) information at high spectral resolution was the Landsat Thematic Mapper (TM). AVHRR, throughout most of its history, only contained red and NIR information. Relating TOA reflectance to surface albedo requires the addition of shorter

wavelengths for characterization of the atmosphere and longer wavelengths for subtle distinctions between snow, soil and vegetation, as shown in Figure 8. Liang et al. (1999) demonstrated through simulations that the kind of spectral information available on a global scale from MODIS would lend itself to a truly robust application of this technique. A neural network was employed toward that end. SASA2 is based on that approach.

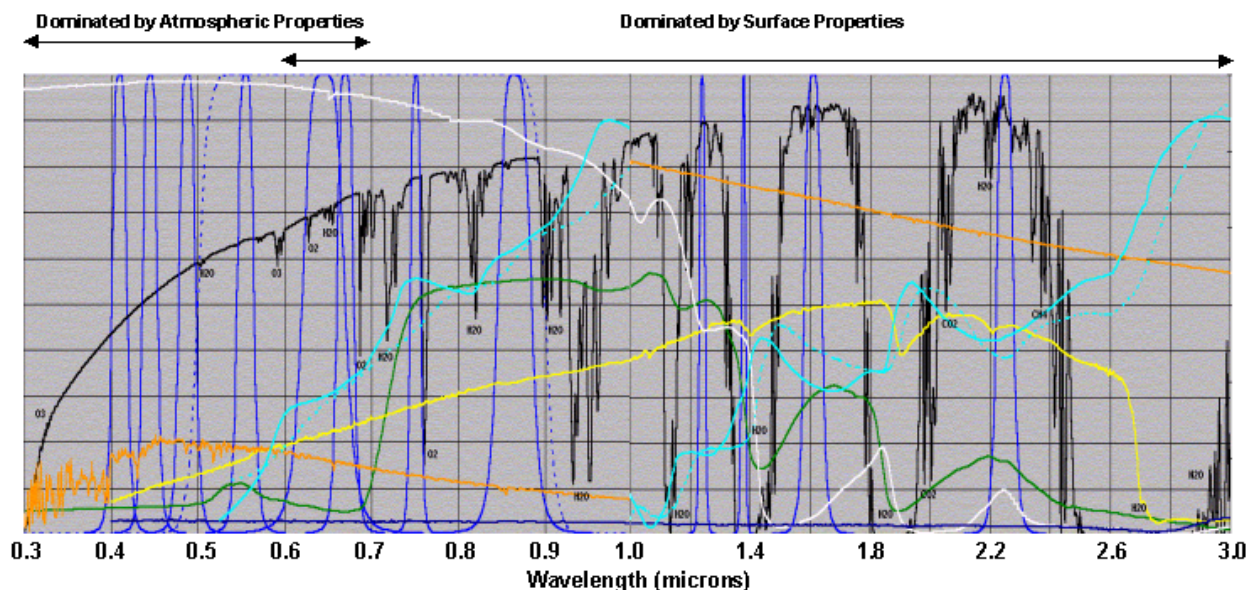


Figure 8. Spectral decoupling of atmospheric and surface properties for derivation of broadband albedo.

The general perception of a neural network is that of a “black box.” This is too broad a generalization, as many of the simpler neural network architectures lend themselves quite readily to physical interpretation of their inner workings. A neural network is essentially a multivariate nonlinear regression equation. Perhaps the best way to develop this concept is by constructing the network one piece at a time.

Consider the following: we take three TOA reflectances— ρ_1 , ρ_2 , and ρ_3 —in different bands, add a constant c_I , and assign a weight w_{hi} , either positive or negative, to each of the four terms, obtaining an estimate of some parameter x_i :

$$x_i = w_{i0}c_I + w_{i1}\rho_1 + w_{i2}\rho_2 + w_{i3}\rho_3 \quad (12)$$

This is a linear regression equation, and its utility is therefore limited to describing relationships that are predominantly linear. Suppose now we nonlinearize the equation by running x_i through a sigmoid function:

$$f(x_i) = \frac{1}{1 + e^{-x_i}} \quad (13)$$

Now we have a new quantity, which we will call H_i :

$$H_1 = f(x_1) = \frac{1}{1 + e^{-(w_{10}c_l + w_{11}\rho_1 + w_{12}\rho_2 + w_{13}\rho_3)}} \quad (14)$$

The structure of the sigmoid function is such that its value always falls between 0 and 1, as shown in Figure 9. For very large positive values of x , $f(x)$ approaches 1, while for very large negative values of x , $f(x)$ approaches 0. Further, $f(0)=0.5$. H_i therefore could be used as an equation for deriving the albedo, and the weights could be treated as regression coefficients toward that end. The nonlinearity might help the algorithm adjust to the nonlinear behavior of surface and atmospheric properties. At best, however, the algorithm will become well-suited to one or two ranges of atmospheric conditions, or one or two general types of surfaces. There are not enough degrees of freedom embodied in the weights to allow a large variety of different behaviors to be modeled, and in particular it is difficult to adequately treat both the atmosphere and surface with this single equation. For example, a very low red reflectance, combined with a high near infrared (NIR) reflectance and a moderate reflectance in the short wave infrared (SWIR), implies healthy or dense vegetation. The atmosphere, however, can distort this relationship. Even moderate amounts of aerosol will raise the red TOA reflectance with respect to the surface, while the NIR reflectance will be lowered, and the SWIR reflectance will be very slightly lowered. These three changes are very similar to differences induced by surface variations: sparse or unhealthy vegetation will also exhibit an increase in the red reflectance combined with a drop in the NIR; the SWIR reflectance will generally tend to increase in this case, due to a loss of water, but this effect is less dramatic than what occurs in the visible and NIR. Another consideration is the weighting of the bands themselves. For snow, most of the solar radiation reflected by the surface is in the visible wavelengths, while for vegetation, most of this radiation is in the NIR. A single equation cannot adequately handle both situations.

Sigmoid Function

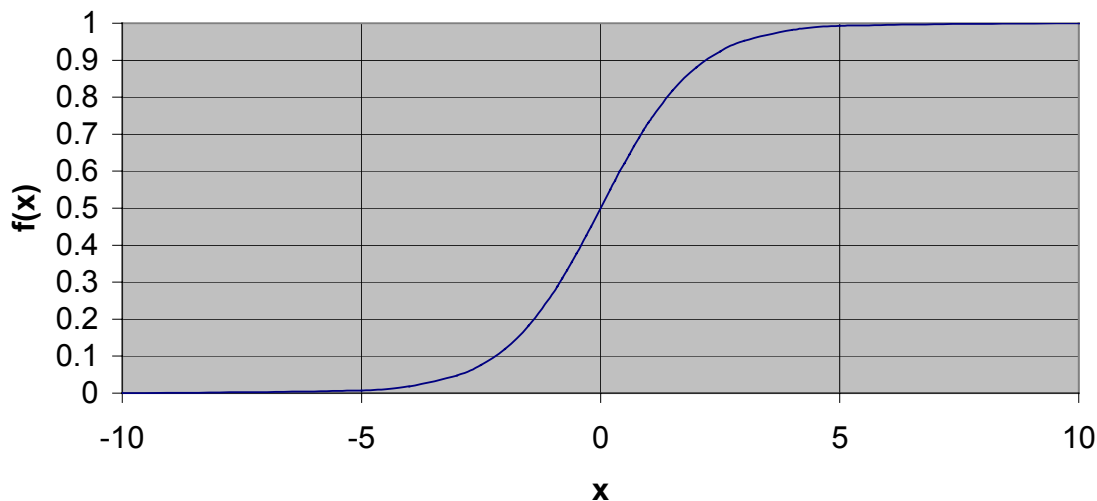


Figure 9. Graph of the sigmoid function, $y=1/(1+e^{-x})$.

Based on these observation, suppose we calculate not one, but three quantities:

$$\begin{aligned}
H_1 &= \frac{1}{1 + e^{-(w_{10}c_I + w_{11}\rho_1 + w_{12}\rho_2 + w_{13}\rho_3)}} \\
H_2 &= \frac{1}{1 + e^{-(w_{20}c_I + w_{21}\rho_1 + w_{22}\rho_2 + w_{23}\rho_3)}} \\
H_3 &= \frac{1}{1 + e^{-(w_{30}c_I + w_{31}\rho_1 + w_{32}\rho_2 + w_{33}\rho_3)}}
\end{aligned} \tag{15}$$

If we were to train these three regression equations on three different surface types or three different kinds of atmospheric conditions, each one would become suited to a particular scenario. In concert, they would comprise a more successful algorithm than a single equation.

Now suppose we do as we did at the beginning with the reflectances, only this time with H :

$$y = c_H + v_1 H_1 + v_2 H_2 + v_3 H_3 \tag{16}$$

This allows us to combine the utility of the three separate equations into one, without losing their independent capabilities. The weights w_{hi} embedded in the terms H_h can be trained to deal with specific situations, while the weights v_h can be trained to determine which situation is applicable. The challenge arises in determining a way to train these coefficients into an optimal configuration.

The system has already been nonlinearized, so we do not need to apply another sigmoid function to y ; instead we can run it through a unity function:

$$g(y) = y \tag{17}$$

Then we can assign this value to the albedo:

$$\begin{aligned}
\alpha &= v_0 c_H + \frac{v_{11}}{1 + e^{-(w_{10}c_I + w_{11}\rho_1 + w_{12}\rho_2 + w_{13}\rho_3)}} \\
&\quad + \frac{v_{21}}{1 + e^{-(w_{20}c_I + w_{21}\rho_1 + w_{22}\rho_2 + w_{23}\rho_3)}} \\
&\quad + \frac{v_{31}}{1 + e^{-(w_{30}c_I + w_{31}\rho_1 + w_{32}\rho_2 + w_{33}\rho_3)}}
\end{aligned} \tag{18}$$

This is a multivariate nonlinear regression equation relating TOA reflectance to surface albedo in a single step. It is also the exact mathematical structure of a three-layer feed-forward neural network. The reflectances, ρ_i , are the inputs. The groups of terms in the parentheses (corresponding to H_h) are hidden nodes (artificial “neurons”), and the final value of the albedo, α , is the output. The weights w_{hi} correspond to connections between the inputs and the hidden nodes, and the weights v_h correspond to connections between the hidden nodes and the output. The sigmoid function used within the hidden nodes is called an activation function, as it is what determines how the node “fires.” This structure is graphically portrayed in Figure 10.

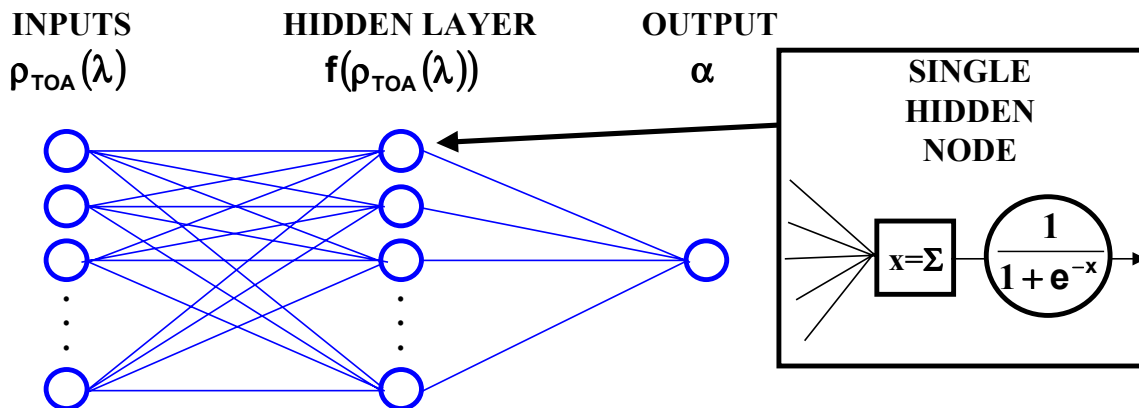


Figure 10. Surface Albedo EDR neural network architecture.

The hidden layer is the heart of a neural network. It is where the network forms what is called its internal representation of the input patterns. This internal representation may not always be decipherable, particularly for very large networks with thousands of inputs and hidden nodes. But for a problem such as albedo retrieval from TOA reflectances, the internal representation can be examined. In general, this type of neural network will have more than one output, interconnected with the hidden layer in much the same way the hidden layer is interconnected with the inputs. In those cases, the output is typically a categorization instead of a quantitative variable. For surface albedo as required here, only one output is needed: the numerical value of the albedo.

The neural network shown in Figure 10 can be trained to estimate surface albedo based on a set of input TOA reflectances. This boils down to a classical optimization problem: the dependent variable is the mean square error between true and retrieved albedo over the training set, and the independent variables are the weights. Classical methods of optimization are difficult to apply, however, because of the sheer number of independent variables involved. Even for the neural network used in our baseline algorithm for surface albedo, there are a hundred weights, meaning the global minimum of the error must be found in a hundred-dimensional space. Matrix methods are not tractable in this instance. The best means of training such a network boils down to a combination of two approaches: conjugate gradients and simulated annealing.

The “learning” process for a neural network such as that pictured in Figure 10 consists primarily of running the network in reverse to obtain partial derivatives of the error with respect to each weight. This technique is called error backpropagation, and it is described in Rumelhart et al. (1986). One of the more robust techniques for using these gradients to find a minimum is that of conjugate gradients. An excellent mathematical description of this technique can be found in Johansson et al. (1992); it essentially approximates the region surrounding a minimum as a quadratic function. A set of mutually orthogonal vectors is then generated to direct the user to the approximate location of the minimum. Conjugate gradients is a fairly “smart” technique; it homes in on the minimum quite rapidly compared to other kinds of backpropagation methodologies.

Conjugate gradients provide an excellent means of zeroing in on a minimum, once it is in the neighborhood. Getting to the neighborhood is more problematic for a scenario with this many dimensions. This is akin to the “traveling salesman” problem, where a salesman has to visit a

hundred cities in the United States, and the aspiring mathematician has to determine which route through the hundred cities corresponds to the shortest overall path. In such situations, the only reasonable solution is one of brute force. Simulated annealing provides this kind of solution. The name for this technique originates in its analogous nature to the physical process of annealing, where a material is treated at successively lower temperatures to produce a strong output product. Simulated annealing involves taking an arbitrary starting point for the independent variables and perturbing them randomly a large number of times with a large standard deviation in the perturbations. The perturbation that produced the lowest error is then selected as a new starting point, about which a new series of perturbations is applied, with a somewhat smaller standard deviation. This process is repeated several times, until the standard deviation, or “temperature,” is sufficiently low to cause minimal change in the error. Once this occurs, conjugate gradients can be applied to refine the weights to a true minimum, and the network is trained. It is not always necessary to find the true global minimum, and in fact even if simulated annealing involves millions of perturbations, the true global minimum might not be found. All that is required is to find a local minimum in the error that meets the user’s requirements. More detail on simulated annealing can be found in Masters (1993) and Press et al. (1989).

The testbed implementation of this process for the Surface Albedo EDR is as follows. A training/testing set is assembled, consisting of a large number of samples. Each sample consists of TOA reflectances in nine bands and the corresponding true surface broadband albedo. Ten percent of the samples are randomly extracted and used to train the network. The network itself has nine inputs plus an input bias, nine hidden nodes plus a hidden bias, and one output, leading to a total of a hundred weights. Simulated annealing is applied, followed by conjugate gradients, until a trained network emerges. This network is then applied to the remaining ninety percent of the training/testing data set, and the performance is recorded to determine if the EDR requirements are met. A summary of the performance of this algorithm is given in Section 3.4.3.6.

It is important to note that the training process is not applied during operational retrievals. Training is performed offline, so that when reflectances are collected, only equation (17), with ten terms (nine reflectance-based plus the constant term) instead of the four shown, need be applied.

No albedo algorithm would be complete without treatment of the BRDF. The original baseline for SASA2 addressed this issue by stratification into angular bins, as shown in Figure 11. For example, a single neural network could be used to handle observations where the solar zenith angle is between 0 and 20 degrees, the viewing zenith is between 20 and 40 degrees, and the relative azimuth is between 0 and 45 degrees. Another network could be used in a different range of angles. This reduces the variability due to BRDF for a given neural network. Unfortunately, the resulting proliferation of separate neural networks, each of which must be trained, requires a vast amount of training data. The updated approach for handling variations due to BRDF is to incorporate the current solar zenith, view zenith, and relative azimuth into the network as additional inputs.

Despite this updated strategy, the largest issue for SASA2 is the assembly of a suitable training set. Simulated data are unlimited in that regard; real data will require a longer period of collection to ensure minimal statistical errors. This issue will be addressed at length in Version 5 of this ATBD.

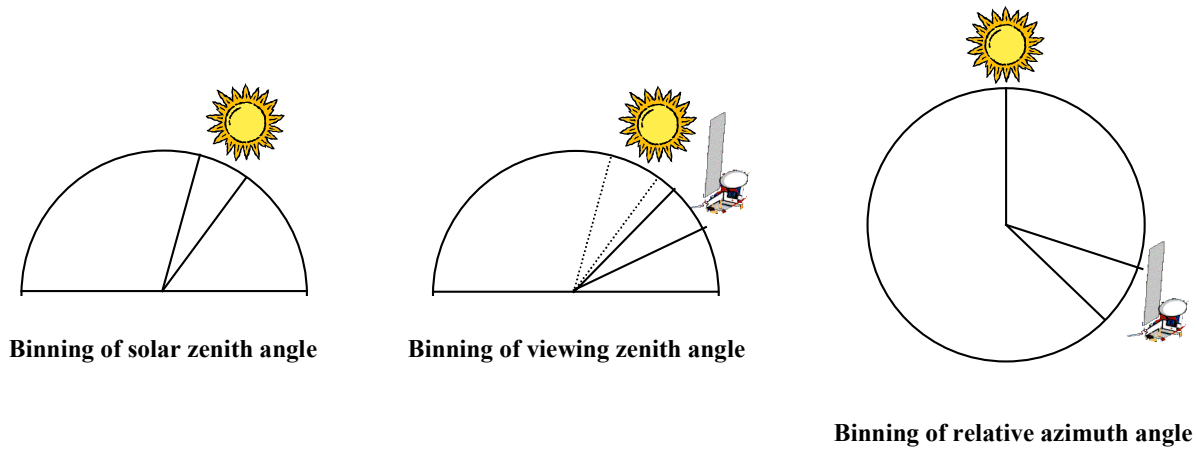


Figure 11. Angular binning to address BRDF variations in the Phase I Surface Albedo EDR algorithm. New baseline replaces this strategy with direct use of three angles as additional inputs to the neural network.

3.4 ALGORITHM SENSITIVITY STUDIES

3.4.1 EDR Requirements

Table 4 lists the requirements from the VIIRS SRD for the Surface Albedo EDR.

Table 4. VIIRS SRD prescribed requirements for the Surface Albedo EDR (TBR = to be reviewed, TBD = to be determined).

Para. No.		Thresholds	Objectives
	a. Horizontal Cell Size		
V40.5.2-10	1. Moderate, worst case	4 km (TBR)	0.5 km
V40.5.2-11	2. Fine, at nadir	1 km (TBR)	0.5 km
V40.5.2-2	b. Horizontal Reporting Interval	(TBD)	(TBD)
V40.5.2-3	c. Horizontal Coverage	Global	Global
V40.5.2-4	d. Measurement Range	0 - 1.0	0 - 1.0
V40.5.2-5	e. Measurement Accuracy (moderate HCS product)	0.05	0.0125
V40.5.2-6	f. Measurement Precision (moderate HCS product)	0.02	0.01
V40.5.2-12	l. Measurement Uncertainty (fine HCS product)	0.03 (TBR)*	(TBD)
V40.5.2-7	g. Long-term Stability	0.02	0.01
V40.5.2-8	h. Mapping Uncertainty	4 km	1.0 km
	i. Maximum Local Average Revisit Time	24 hrs	4 hrs
	j. Maximum Local Refresh	(TBD)	(TBD)
V40.5.2-9	k. Minimum Swath Width (All other EDR thresholds met)	3000 km (TBR)	(TBD)

The SRD requirements set the limits for an error budget in the Surface Albedo EDR. There are four crucial parameters in Table 4 that directly constrain the allowable errors in the Surface Albedo: accuracy, precision, uncertainty, and long term stability. Appendix A of the VIIRS SRD defines these primary metrics for assessment of EDR algorithm performance.

Note that there are really two products required by the SRD: a moderate resolution Surface Albedo driven by edge-of-scan performance, and a fine resolution Surface Albedo driven by nadir performance. Our solution for this EDR produces a single Surface Albedo product to satisfy the moderate and fine requirements, with a nadir resolution of 750 m, growing to a resolution of 1600 m at the edge of the scan.

3.4.2 Performance Metrics

Consider a single true value T of an EDR product at the HCS. A satellite-borne sensor will produce data which can be transformed through a retrieval algorithm into an estimate X_i of T , where the index i indicates that any arbitrary number N of such estimates can be made. Various error sources along the pipeline between the true value T and the measured value X_i will cause X_i to deviate from T . The accuracy A_{SRD} is defined in the VIIRS SRD as:

$$A_{SRD} = |\mu - T| \quad (19)$$

where μ is the average of all the measured values X_i corresponding to a single true value T :

$$\mu = \frac{1}{N} \sum_{i=1}^N X_i \quad (20)$$

The accuracy can therefore also be termed as a bias, and is a direct comparison between the measurements X_i and the true value T .

The precision P_{SRD} is defined in the SRD as the standard deviation of the measurements:

$$P_{SRD} = \left(\frac{1}{N-1} \sum_{i=1}^N (X_i - \mu)^2 \right)^{1/2} \quad (21)$$

Thus, the actual calculation of the precision as defined in the SRD is completely independent of the true value T , however it is important to keep in mind that the precision is still defined only for measurements corresponding to a single value of T . Were this not so, P_{SRD} would describe only the natural variability of the parameter being measured, and this would preclude its use as a measure of algorithm performance.

The uncertainty U is defined as:

$$U_{SRD} = \left(\frac{1}{N} \sum_{i=1}^N (X_i - \mu)^2 \right)^{1/2} \quad (22)$$

The uncertainty is therefore alternatively known as the root mean square (RMS) error between the measurements X_i and the true value T .

As mentioned in the SRD, the definitions of accuracy, precision, and uncertainty given in Equations (19), (21), and (22), respectively, are idealized, because they assume a single value of T . In reality, this cannot be implemented, because there are an infinite number of possible values

for T , each possible value is likely to be manifested as truth only once, and we cannot hope to pinpoint T to arbitrary accuracy. The practical implementation of the SRD definitions is to bin the possible values of T into small ranges that are large enough to provide a statistically significant number of test points but small enough to ensure the metrics are not dominated by natural variability. The simplest result would be a modification of equations (19), (21), and (22) into the following:

$$A = |\mu - \mu_T| \quad (23)$$

$$P' = \left(\frac{1}{N-1} \sum_{i=1}^N (X_i - \mu)^2 \right)^{1/2} \quad (24)$$

$$U = \left(\frac{1}{N} \sum_{i=1}^N (X_i - T_i)^2 \right)^{1/2} \quad (25)$$

Thus, precision P' would be identical to P_{SRD} , only it is understood that P' now corresponds to some small range of true values T_i , instead of one true value T . The single value of T in the accuracy definition is now changed to the mean of the true values T_i within some small range, and the single value of T in the uncertainty definition is now changed to the particular true value T_i corresponding to the measurement X_i .

Equations (23), (24), and (25) now exactly correspond to the bias, standard deviation of the measurements, and RMS error, respectively. These are all quite common statistical measures. The accuracy A will give a clear indication of any biases in the processing pipeline for a given EDR, and the uncertainty U will provide a good measure of overall error. A problem arises, however, in using P' as a metric for evaluating retrieval errors. Since P' corresponds to a small range of true values T_i , but it does not explicitly account for the variations in T_i , it now includes the natural variability of the parameter being measured. In fact, without incorporating the true values T_i into the equation, P' becomes ambiguous.

Consider, as an example, the effects of band-to-band misregistration on the Surface Albedo EDR. The following would apply for some small range of true values, say from 0.40 to 0.42. "Truth" would be an albedo value within this range for a horizontal cell in which the input bands are completely overlapping. An ensemble of true values T_i could then be created using a two dimensional Landsat TM scene. For each of these horizontal cells, the near infrared band could then be shifted 30 meters to the right with respect to the other bands, and new "measured" values X_i of the albedo could be obtained to match up with the true values T_i . These measured values X_i could be plugged into Equation (24) to obtain an estimate of the precision for 30-m misregistration. The process could then be repeated for 60-m misregistration.

But note that nowhere do the true values T_i enter into Equation (24). The result is that the precision for the 60-m misregistration scenario is likely to be almost exactly the same as the precision for the 30-m misregistration scenario, because it is only a measure of the variability within the scene. Additionally, precision as defined by P' is a strong function of bin size. If the albedo is binned into ranges that are 0.1 albedo units wide, the precision for each bin will become much higher, because the truth varies over a broader range.

P_{SRD} is a very useful metric for data points which correspond to a single value of truth T , such as in simulations conducted for sensor signal to noise ratio (SNR). But for spatial and temporal fields of truth T_i which must be binned into small ranges, P' fails as an extension of P_{SRD} . It is therefore recommended in these special situations that the precision definition P' be replaced by a system-level expression that ensures uncertainty is the root sum square of accuracy and precision:

$$P = (U^2 - A^2)^{1/2} \quad (26)$$

In other words, precision P now corresponds to the bias-adjusted RMS error for situations with variable truth. This provides a metric that captures the spread of the measurements about the truth, with the bias associated with the accuracy metric removed to distinguish it from the total error given by the uncertainty. Further, P is not a strong function of bin size; P for a large range of albedo values is roughly equivalent to the average of P for several smaller ranges within the large range. Finally, Equation (26) is explicitly called out in the SRD as a limiting relationship for A , P , and U when the number of observations in a given bin becomes very large.

3.4.3 Individual Error Sources

The following sections discuss the major error sources for the Surface Albedo EDR.

3.4.3.1 Phase I Sensor Error Evaluations

Phase I activities included a necessary look at the flowdown of EDR requirements to algorithm data definitions (ADDs) for the output of the sensor. These included dynamic range, radiometric calibration and sensitivity, spatial resolution, polarization characteristics, and so forth. Because of the demanding requirements for other products, such as Ocean Color, Sea Surface Temperature, and Imagery, Surface Albedo was not the single driver for any of these parameters. The major sensor error sources will now be discussed in brief, however, to provide further context for the error budget. The following discussion focuses primarily on the algorithms that were developed in Phase I trade studies; sensor impacts on the adapted MODIS approach (SASA1) will be detailed in a later version of this document.

3.4.3.1.1 Sensor Noise

A real sensor, even if perfectly calibrated, will convert a true top-of-atmosphere (TOA) radiance to a corresponding measured radiance that departs from the truth by some random amount, leading to noise in an ensemble of measurements. The major contributors to sensor noise are: photon or "shot" noise, caused by natural variations in the number of photons striking the instrument; detector and electronics noise, typically constant for a given detector; and quantization noise, caused by the conversion of continuous radiance into a finite number of bits.

On the whole, sensor noise can be treated with good fidelity as Gaussian. This assumption breaks down at the limits of the sensor's dynamic range, however it was sufficiently accurate for flowdown of sensor noise requirements at specified radiances. The reader is directed to Hucks (1998) for a more detailed description of the sensor noise modeling process. It is only briefly summarized here. The VIIRS radiometric performance model describes the sensor noise as a function of TOA band radiance, N_{TOA} as,

$$\sigma = \sqrt{\alpha N_{TOA} + \beta} \quad (27)$$

where N_{TOA} , a band radiance in units of $\text{Wm}^{-2}\text{sr}^{-1}$, is chosen as a naming convention to differentiate it from L_{TOA} , the spectral radiance in $\text{Wm}^{-2}\text{sr}^{-1}\mu\text{m}^{-1}$. The quantity σ is the standard deviation of the signal caused by sensor noise, assuming a Gaussian distribution. The values α and β are two constants derived from the numerous physical quantities associated with sensor noise, including measured detector characterizations, integration time, instantaneous field of view (IFOV), optical throughput, and so forth. In Phase I, we applied these constants as supplied by SBRS for the specified level of sensor noise in the appropriate bands, and the resulting errors were found to be negligible for the Surface Reflectance IP, typically on the order of 0.005 reflectance units or less. The only band significantly affected by sensor noise is band I3, an imagery-resolution band in a region of the spectrum where the solar signal is relatively low. Aggregation of this band to moderate resolution, however, cuts the noise in half and renders the band sufficiently sensitive for use by the appropriate downstream retrieval algorithms.

When SASA2 was adopted as the baseline algorithm for the Surface Albedo EDR, the sensor noise error term was folded into the TOA reflectance error, discussed in Section 3.4.3.5. These results confirmed that sensor noise has negligible effects on the Surface Albedo EDR, due to the very low-noise performance of the VIIRS driven by other EDRs. A similar situation exists for MODIS, so that radiometric calibration is considered the only significant sensor error source for the MODIS albedo algorithm. This will be succinctly verified for SASA1 in the VIIRS context, and the results will be presented in Version 5 of this ATBD. The analyses already conducted for the Surface Reflectance IP [Y2411] in Phase I suggest that SASA1 will be insensitive to sensor noise errors from the VIIRS.

3.4.3.1.2 Radiometric Calibration

The VIIRS Sensor Specification [PS154650] for the upper bound on radiometric calibration accuracy is 2% in the reflective bands. This was largely driven by ocean and aerosol requirements. Since Surface Albedo is a global EDR, i.e., it must be retrieved over oceans as well as land, this flowdown has some relevance to the present discussion. The absolute nature of the Surface Albedo EDR requirements, however, allows significantly more room for relative error than is the case for ocean and aerosol products. In fact, from the standpoint of meeting the EDR requirements, the most significant impacts of sensor calibration errors for Surface Albedo occur for the brightest surfaces, especially snow. For these surfaces, SASA2 is employed to retrieve the Surface Albedo EDR, and so calibration errors are folded into TOA reflectance error, which is discussed in Section 3.4.3.5. For SASA1, the MODIS heritage assessment of calibration accuracy impacts on albedo retrievals has not yet been completed; any findings available in time for inclusion in Version 5 of this ATBD will be incorporated into that document. It is expected that both MODIS and VIIRS possess sufficiently tight specifications on radiometric accuracy

that the performance of albedo retrieval algorithms over dark surfaces will be sufficient to meet the product-level requirements.

3.4.3.1.3 MTF Effects

The most likely scientific interpretation of a “perfect” pixel would be one that perfectly represented the averaged radiance over some square region on the Earth’s surface. The average should be equally weighted across the entire square, with no contributions from outside the borders. In reality, of course, this is not achieved. A pixel will instead be the result of several convolutions, due to scattered and stray light, diffraction, blurring, the finite nature of the detector, and so forth. This will have the effects of varying the weighting within the target region on the surface and incorporating photons which came from outside this region, either from surrounding regions on the surface or from entirely different sources such as clouds. The ultimate effect of all these convolutions can be represented as the sensor point spread function (PSF), which typically has some central peak near the center of the target region, around which the radiances contributed from surrounding areas of the Earth’s surface drop off in a typically exponential manner. The Modulation Transfer Function (MTF) is defined as the magnitude of the Fourier transform of the PSF.

There is some debate as to whether the deviation of a real sensor PSF from a "boxcar" idealized pixel is a real error. For verification purposes, the issue is moot, since ground measurements will not match the sensor PSF or the boxcar. Phase I did include a look at MTF errors for a simplified, Lambertian-based, linear regression approach to albedo retrievals, and the EDR was found not to be the most significant driver. In fact, Vegetation Index [Y2400] was a much stronger driver. Both EDRs, however, can benefit from the presence of three reflective bands on VIIRS at imagery resolution: I1, I2, and I3. I1 is driven by Imagery EDR requirements. I2 and I3 were added to address the high-resolution requirements for NDVI and Snow Cover. These three bands, as shown for example in Section 3.4.3.4, contain the lion's share of information about surface characteristics for the retrieval of land parameters such as albedo. Additionally, not only are these bands at higher resolution, allowing aggregation to reduce their MTF errors, but they also have a sharper PSF to begin with, in order to provide maximum benefit to the Imagery EDR. MTF error is therefore expected to be a minor component of the Surface Albedo error budget.

3.4.3.1.4 Band to Band Registration

Any two given bands on the VIIRS instrument would ideally project to perfectly aligned pixels at the same spot on the ground. In reality, any two given bands will be offset in an arbitrary direction from one another, causing errors in EDR retrieval algorithms.

As with MTF errors, this issue was considered early in Phase I for Surface Albedo, for a simplified algorithm that is no longer part of the baseline, and again Surface Albedo was not as significant a driver as other EDRs. Also as with MTF errors, Surface Albedo benefits from the presence of the imagery-resolution bands I1, I2, and I3. I1 and I2 have been driven to 80% or more spatial overlap by the Vegetation Index EDR, and because of the VIIRS design strategy, I3 is expected to be well aligned with I1 and I2. Additionally, these bands are aggregated in the Surface Albedo EDR approach, further reducing misregistration errors. As a result, band to band registration is expected to be a minor component of the Surface Albedo error budget.

3.4.3.2 Atmospheric Correction Errors

There are four major sources of atmospheric noise in the reflective portion of the spectrum: water vapor absorption, ozone absorption, Rayleigh scattering, and aerosol extinction. For the reflective bandwidths on VIIRS, ozone and water vapor absorption sensitivity is minimal, as gaseous absorption features have been avoided, and the available ancillary data are sufficiently accurate to robustly remove the effects on TOA radiance. Rayleigh scattering and aerosol effects are typically on the same order, and both decrease in importance moving toward longer wavelengths. Because of their variability, aerosols are the dominant error source for the Surface Reflectance IP. The Surface Reflectance algorithm internal to the VIIRS pipeline is based upon the MODIS atmospheric correction product (Vermote and Vermeulen, 1999). In both products, all four of the above sources of atmospheric noise are handled. Additionally, BRDF/atmospheric coupling effects are taken into account, and a placeholder exists for the eventual handling of adjacency effects. For details on sources and magnitudes of errors in the Surface Reflectance IP, and for a summary of overall performance, the reader is directed to [Y2411]. The flowdown of these errors into SASA1 are discussed in some detail in Lucht *et al.* (2000), including the errors involved in the diffuse skylight computation. Lewis and Barnsley (1994) found this approximation to be on the order of only a few percent even for low solar zenith angles, where the direct beam is most dominant. Further details for VIIRS will be presented in Version 5 of this ATBD, however since MODIS and VIIRS are spectrally and radiometrically similar, the differences are expected to be minimal.

Since SASA2 utilizes TOA reflectance instead of surface reflectance, atmospheric correction error is not a term in the error budget for that algorithm. Atmospheric variability, on the other hand, does play a significant role. Variability on a local scale is generally fairly small, however variability on a global basis for the implementation of a single algorithm feeds into Surface Albedo precision error. This effect is absorbed into the algorithmic error for the SASA2, which is described in Section 3.4.3.6.

3.4.3.3 BRDF Effects

The magnitude of the errors associated with BRDF approximation for SASA1 are described in the context of MODIS retrievals by Lucht *et al.* (2000). A discussion of extending these results to the VIIRS algorithm will be presented in Version 5 of this ATBD. Further assessment of the BRDF modeling performance will leverage the validation efforts for MODIS. Early results, such as those presented at the January 2001 MODIS Land Science Team Meeting, suggest that the BRDF modeling is stable and capable of meeting the VIIRS requirements for dark surfaces.

For SASA2, these errors are folded into the algorithmic error, which is described in Section 3.4.3.6. The simulations conducted thus far, however, assumed a Lambertian surface, and so the assessment of BRDF errors for SASA2 is still pending. Sensitivity studies will be conducted in Phase II to assess the magnitude of these errors, and the preliminary results will be provided in Version 5 of this ATBD. Ultimately, SASA2 will need to be validated using real satellite and validation data, and this effort will draw heavily from the MODIS and international infrastructures for albedo algorithm validation.

3.4.3.4 Narrow to Broadband Conversion

The conversion from spectral to broadband albedo, depends on several factors. These include: the atmospheric state; the underlying surface type; the number of chosen spectral bands; the band specifications (bandcenter, bandwidth, filter function); and the chosen associated weights or coefficients for the conversion.

Early in Phase I, a number of different albedo retrieval algorithms were considered. One was a Lambertian-based linear regression approach, the primary benefit of which is extreme ease of use in an operational setting. The narrow to broadband conversion issue was investigated for this approach, and the results are deemed sufficiently relevant to be included in this ATBD. In order to evaluate the performance of the Lambertian-based algorithm, several surface types—vegetation, soil, snow and water—were simulated using data from the ASTER Spectral Library (<http://speclib.jpl.nasa.gov>). All atmospheric simulations were performed using the 6S radiative transfer code (Vermote *et al.*, 1997). The US Standard atmosphere was employed for all the simulations. The investigated combinations of VIIRS, MODIS, and AVHRR bands are listed in Table 5. Most of these are listed in Table 2. Also investigated were bands M6 (746 nm, used for atmospheric correction over oceans), M9 (1.38 μm , used for cirrus and stratospheric aerosol retrievals), MODIS band 6 (1.64 μm), and AVHRR bands 1 and 2. This was part of early efforts to verify the appropriateness of the baseline VIIRS spectral ranges.

Table 5. Indexed combinations of channels considered for conversion from narrow to broadband albedo for Phase I evaluation of the Lambertian-based regression algorithm.

Combination	Set of Bands Used
1	M1, M2, M3, M4, I1, M6, I2, M8, M9, I3, M11
2	Same as 1, but without M9 (1.38 μm)
3	Same as 1, but without M6 (746 nm)
4	Same as 1, but without M6 or M9
5	M3, M4, I1, I2, M8, I3, M11
6	M3, M4, I1, I2, I3, M11
7	M3, M4, I1, I2, MODIS band 6 (1.628-1.652 μm), M11
8	M3, M4, I1, I2, MODIS band 6 (1.628-1.652 μm), M8, M11
9	AVHRR bands 1 (572-703 nm) and 2 (720-1000 nm)
10	M4, I1, I2, MODIS band 6 (1.628-1.652 μm), M11
11	I1, I2, MODIS band 6 (1.628-1.652 μm), M11
12	M4, I2, MODIS band 6 (1.628-1.652 μm), M11
13	I1, I2, M11
14	I1, I2, MODIS band 6 (1.628-1.652 μm)
15	I1, I2, I3

Figure 12 illustrates the errors using the various combinations of spectral bands. A number of observations can be made. First, the minimum error is obtained using combination 5, which corresponds roughly to the Landsat Thematic Mapper (TM) bandset. The SASA2 baseline for VIIRS uses these bands plus M1 and M2 to increase information about atmospheric scattering. For the purpose of data continuity, a comparison between VIIRS and AVHRR derived albedo is

also of interest. The narrow to broadband conversion using only the red and near infrared bands (combination 9) shows reasonable results for all surface types but snow, where the VIIRS performs considerably better than the AVHRR. The most recent heritage for AVHRR includes a switchable band at $1.61\ \mu\text{m}$ —the same wavelength as for VIIRS band I3—which should improve performance. In fact, combination 15—the three imagery-resolution reflective bands for VIIRS—yields reasonable results for all surface types. This suggests most of the important spectral information characterizing the surface can be found in these three bands.

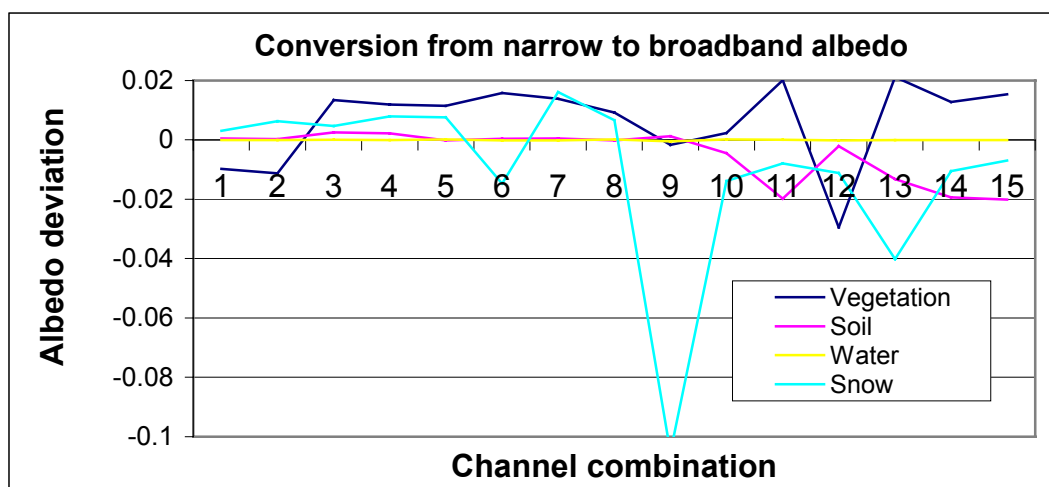


Figure 12. Narrow to broadband albedo conversion errors from Phase I evaluation of a Lambertian-based linear regression algorithm, using the combinations of channels listed in Table 9 for four different backgrounds.

For SASA1, narrow to broadband conversion is accomplished using the coefficients developed for MODIS bands by Liang *et al.* (1999); the reader is directed to that document for a discussion of the errors involved. Sensitivity studies for this approach as applied to VIIRS will be presented in a later version of this document. Since the VIIRS bands are quite similar to their MODIS counterparts, large differences in performance are not expected.

3.4.3.5 TOA Reflectance Errors

The primary input to SASA2 is TOA reflectance. Consequently, the stratified performance for TOA reflectance in the relevant bands was investigated in Phase I using a large ensemble of “stick model” simulations—successive single-point executions of MODTRAN3.7 using various viewing and solar geometries, aerosol properties, and surface types. The dimensions of this data set are summarized in Table 6.

Table 6. Summary of dimensions for the Phase I TOA Reflectance and SASA2 stick modeling data set.

Parameter	# Different Values	Range
Surface Type	10	Coniferous forest, deciduous forest, shrub, grass, crops, urban, snow, bare soil, desert sand, water
Solar Zenith	8	0-70 degrees
Scan Angle	7	0-60 degrees
Relative Azimuth	5	0-180 degrees
Aerosol Type	4	Urban, rural, desert, LOWTRAN maritime
Aerosol Optical Thickness	5	0.1-0.5

All forward modeling was conducted using MODTRAN 3.7, with a midlatitude summer profile. It was not deemed necessary to vary the profile, as water vapor, temperature, and ozone effects are much smaller than the effects of aerosols in the VIIRS bands used for reflectance-based land EDRs. The output of each stick model simulation consisted of a true broadband surface albedo, true TOA reflectances in the nine spectral bands from Table 2, and true surface reflectances in these same bands. Sensor noise for the VIIRS sensor was simulated using the methodology briefly described in Section 3.4.3.1.1. The constants α and β were set corresponding roughly to the sensor specification for the various bands required by the Surface Albedo EDR. These were combined with a simulated value of 2% reflectance calibration accuracy across all bands to give the performance results plotted in Figure 13 through Figure 21. For each of these plots, the accuracy originates with the calibration errors, and the precision originates with sensor noise. It is clear from these plots that sensor noise is negligible for the purposes of SASA2, and that calibration errors are minor except for bright surfaces, primarily snow and desert. As shall be seen in Section 3.4.3.6, even with the specified calibration errors over snow and desert, SASA2 appears to meet the threshold accuracy requirement of 0.05 for all conditions.

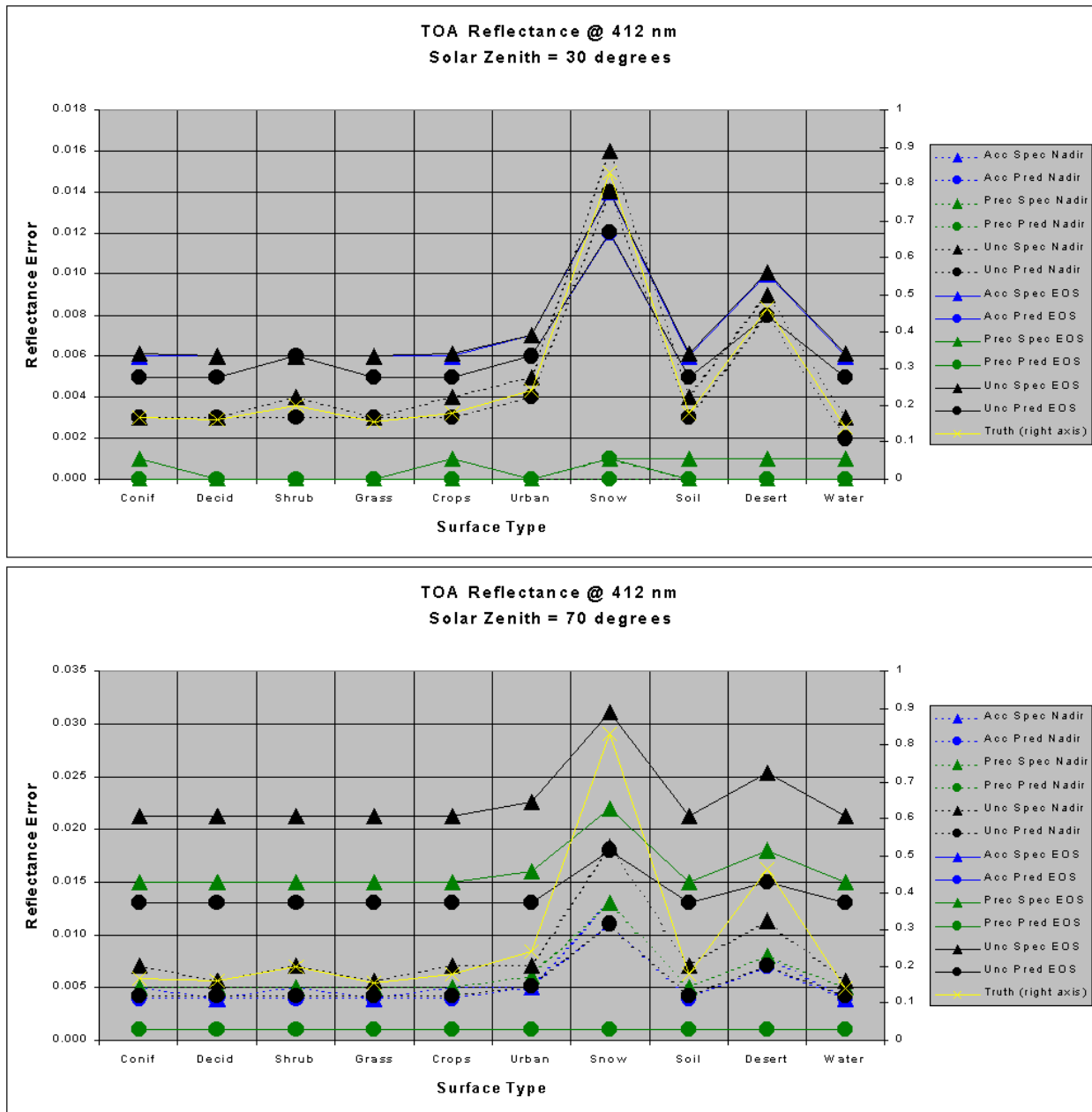


Figure 13. TOA reflectance errors at 412 nm, for nadir and edge of scan, at solar zenith of 30 degrees (top) and 70 degrees (bottom), using both specified and predicted sensor performance as input.

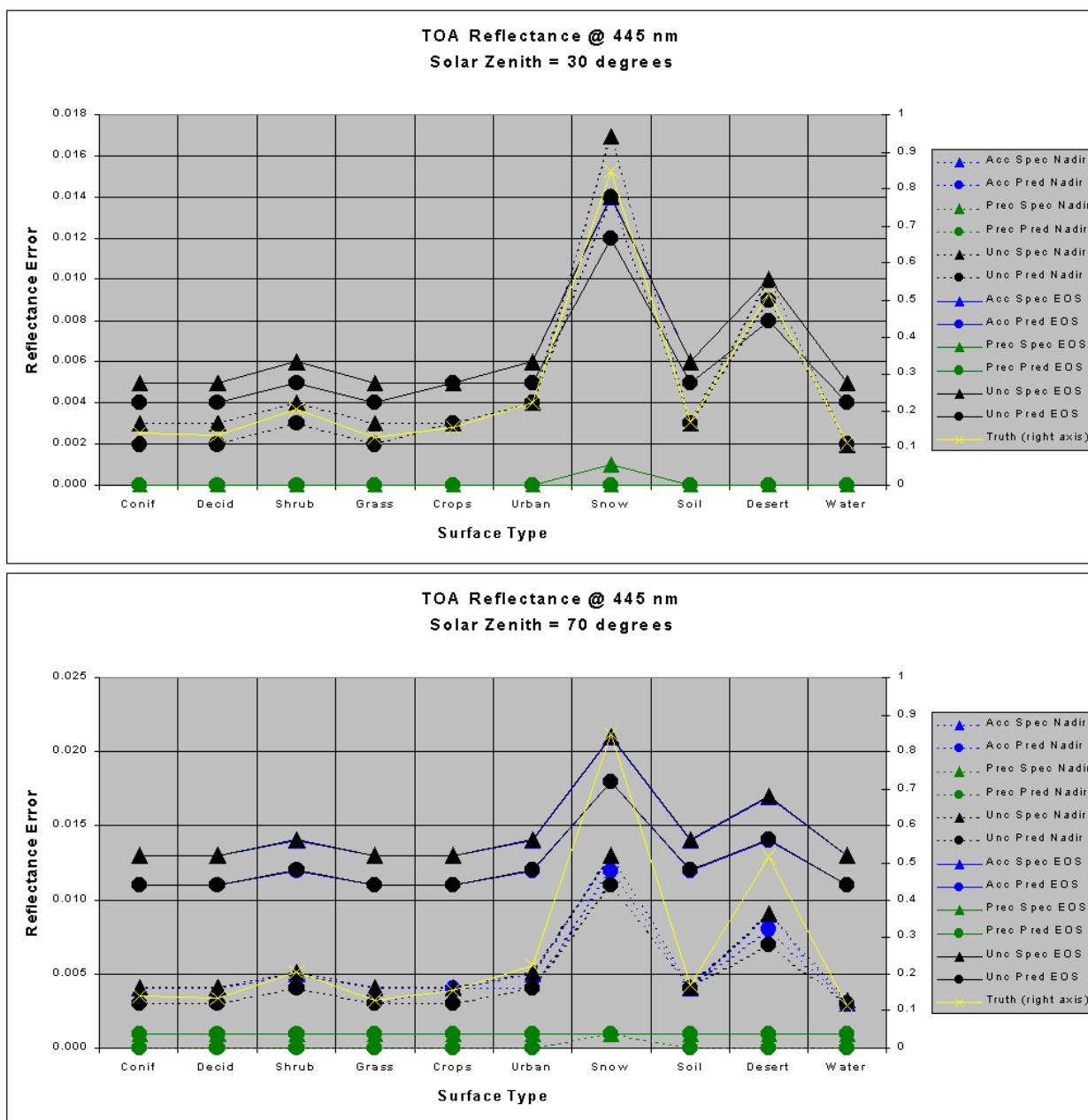


Figure 14. TOA reflectance errors at 445 nm, for nadir and edge of scan, at solar zenith of 30 degrees (top) and 70 degrees (bottom), using both specified and predicted sensor performance as input.

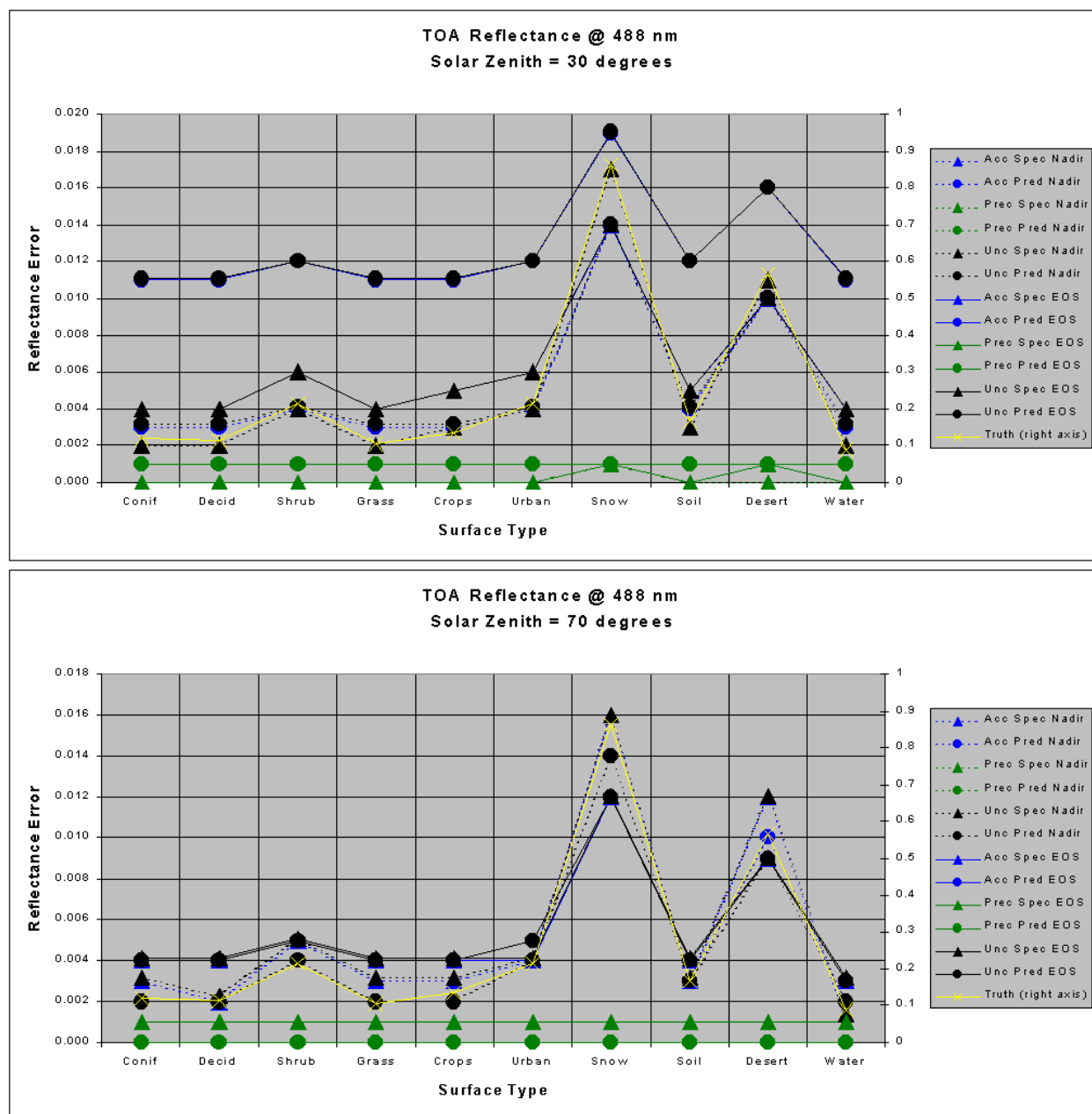


Figure 15. TOA reflectance errors at 488 nm, for nadir and edge of scan, at solar zenith of 30 degrees (top) and 70 degrees (bottom), using both specified and predicted sensor performance as input.

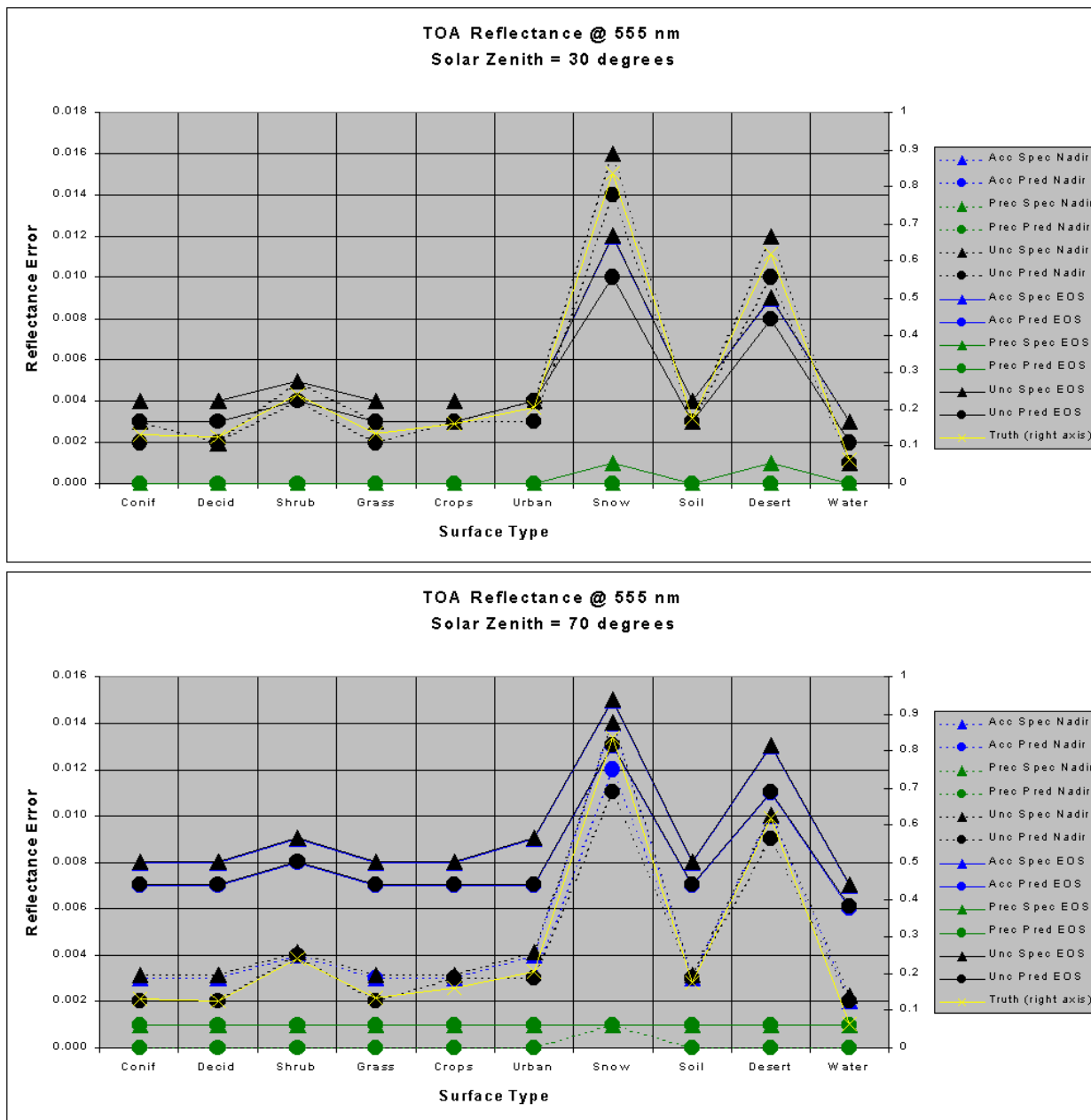


Figure 16. TOA reflectance errors at 555 nm, for nadir and edge of scan, at solar zenith of 30 degrees (top) and 70 degrees (bottom), using both specified and predicted sensor performance as input.

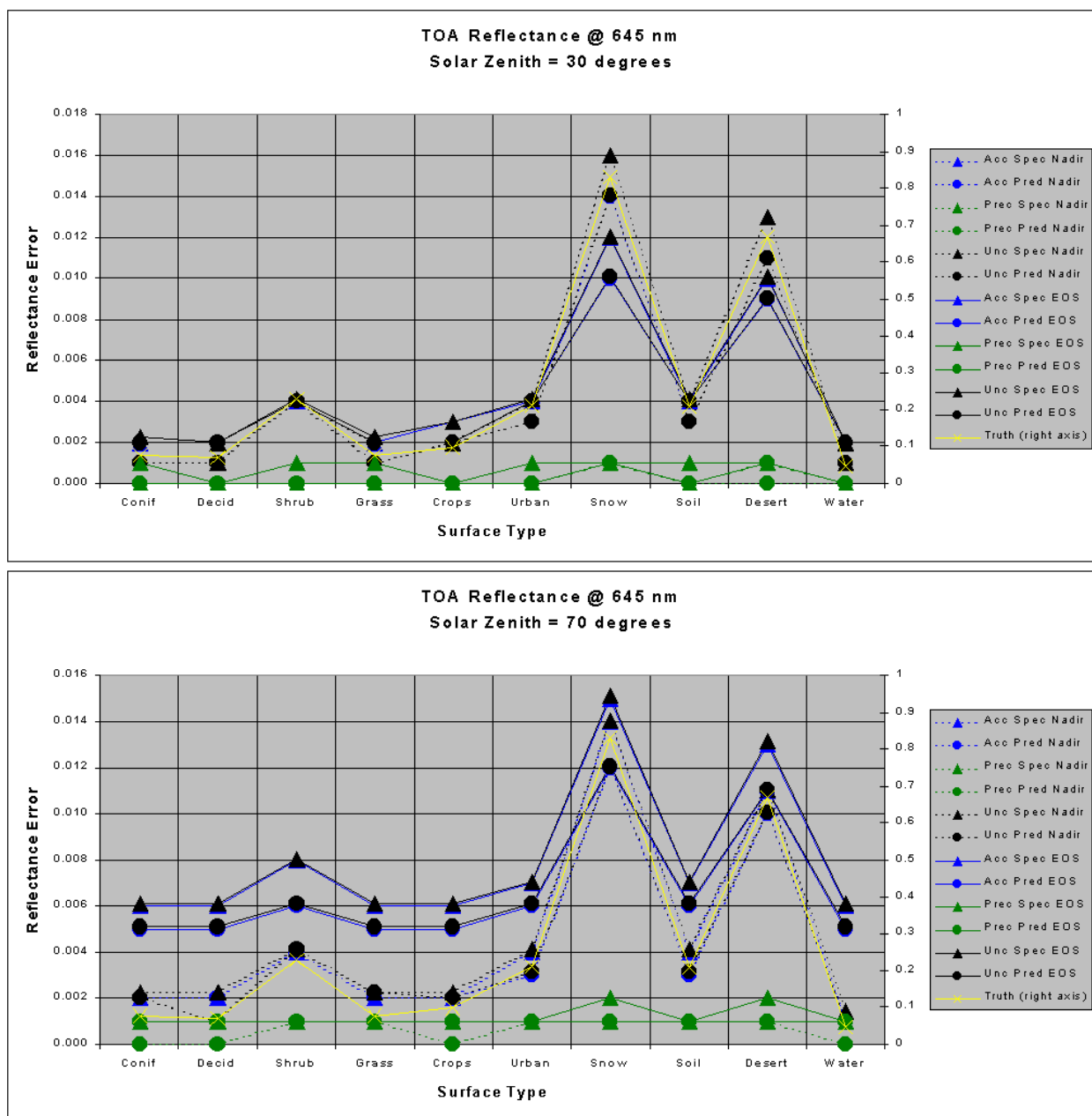


Figure 17. TOA reflectance errors at 645 nm, for nadir and edge of scan, at solar zenith of 30 degrees (top) and 70 degrees (bottom), using both specified and predicted sensor performance as input.

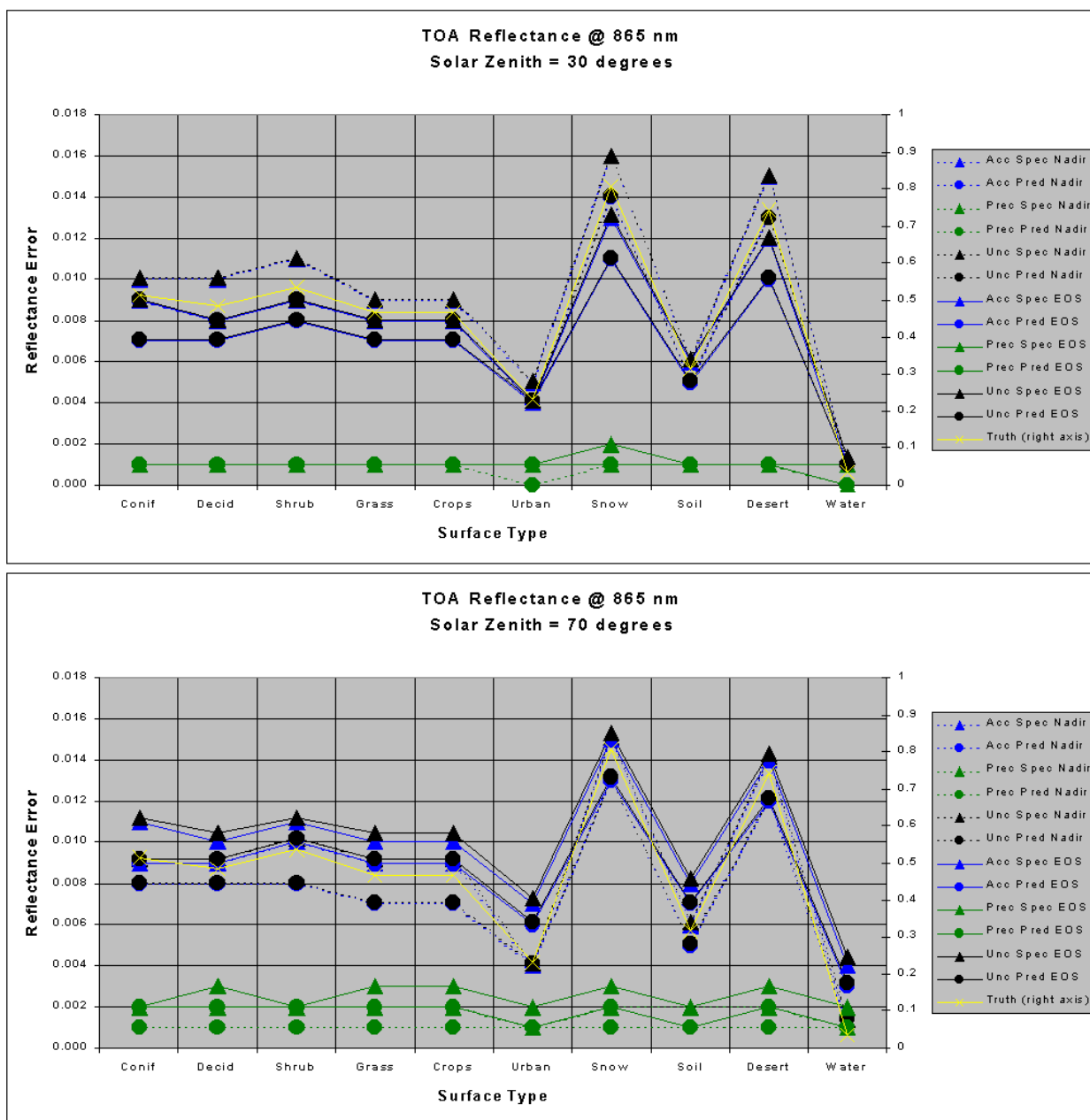


Figure 18. TOA reflectance errors at 865 nm, for nadir and edge of scan, at solar zenith of 30 degrees (top) and 70 degrees (bottom), using both specified and predicted sensor performance as input.

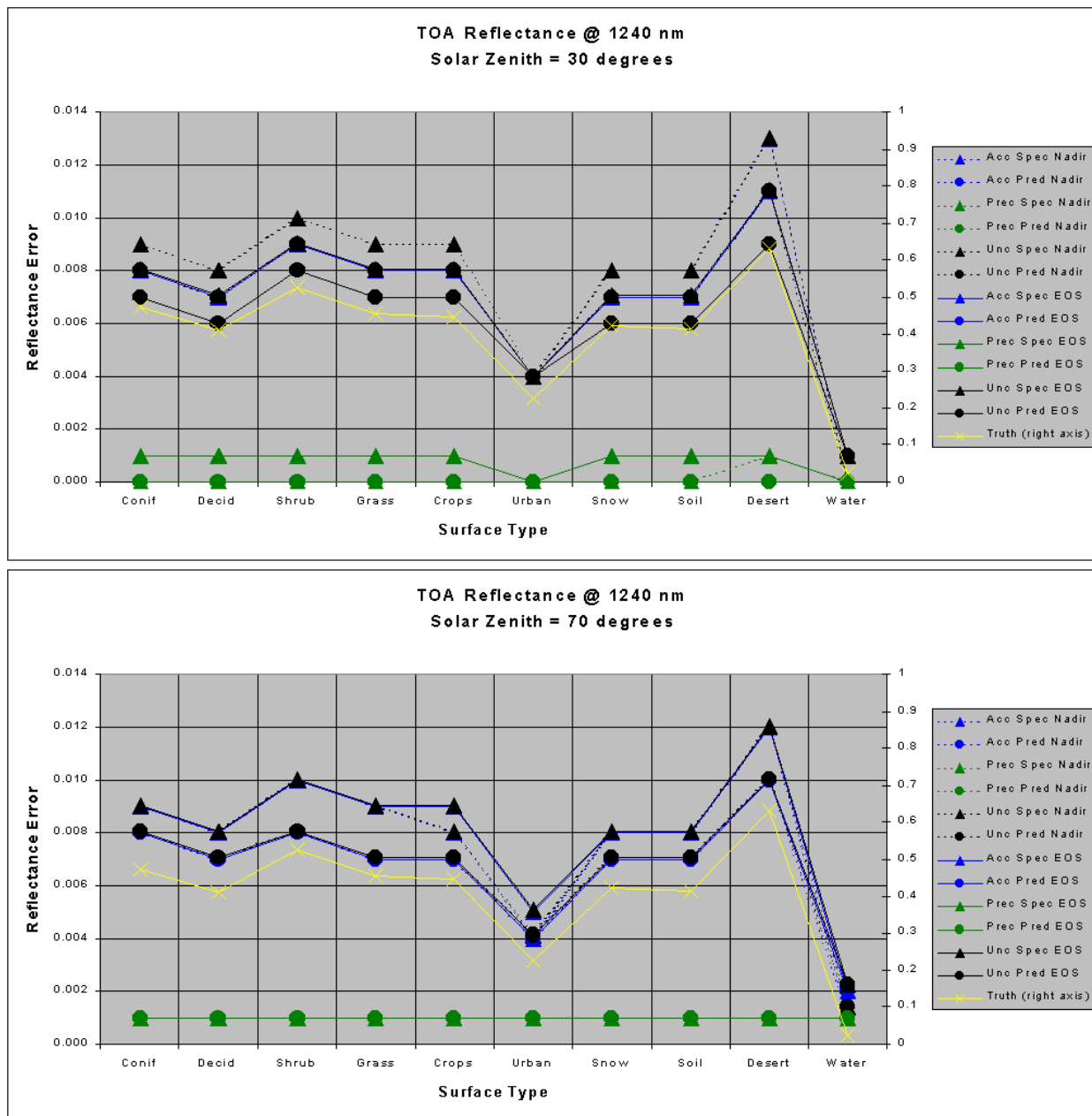


Figure 19. TOA reflectance errors at 1240 nm, for nadir and edge of scan, at solar zenith of 30 degrees (top) and 70 degrees (bottom), using both specified and predicted sensor performance as input.

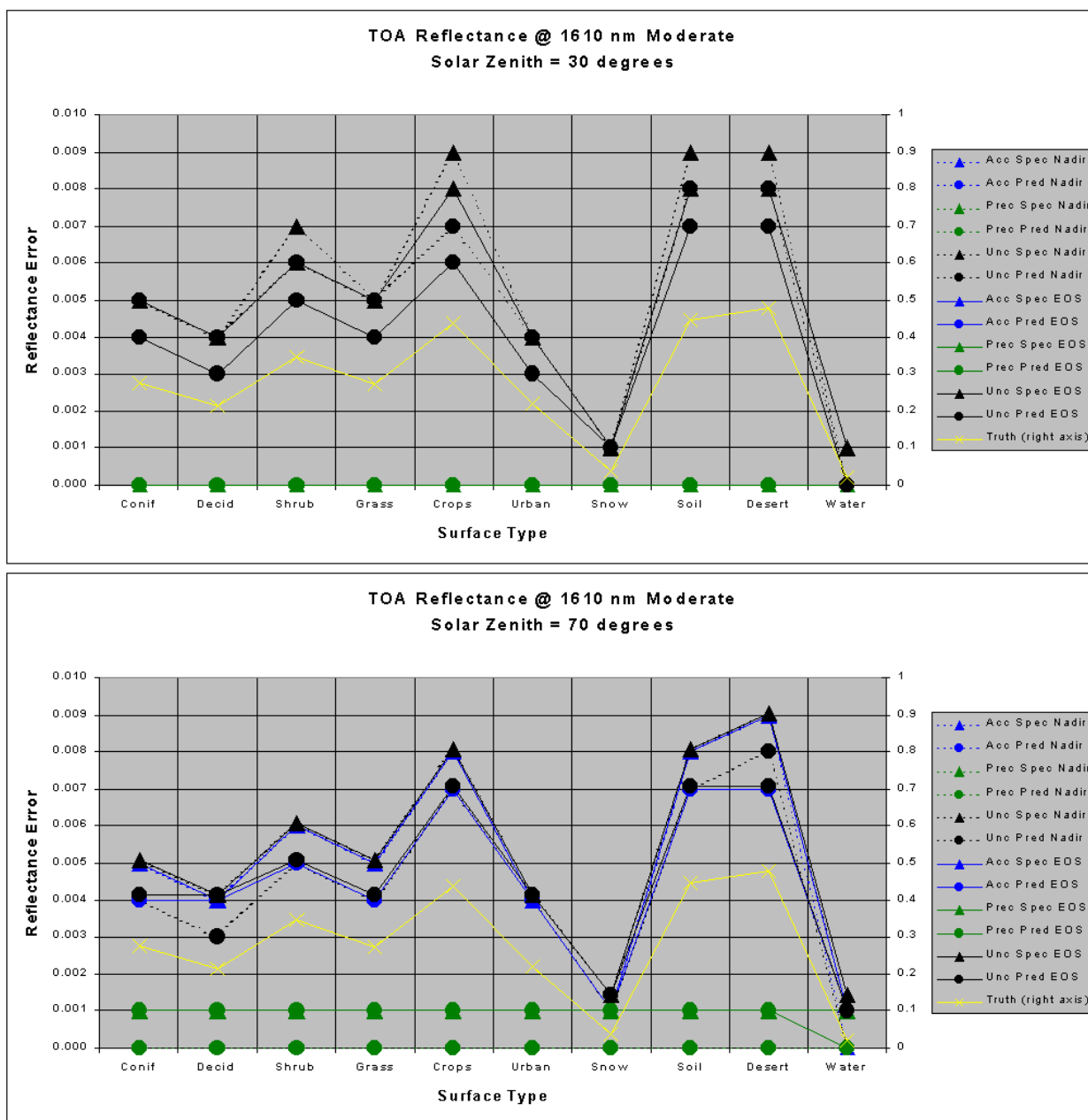


Figure 20. TOA reflectance errors at 1610 nm, for nadir and edge of scan, at solar zenith of 30 degrees (top) and 70 degrees (bottom), using both specified and predicted sensor performance as input.

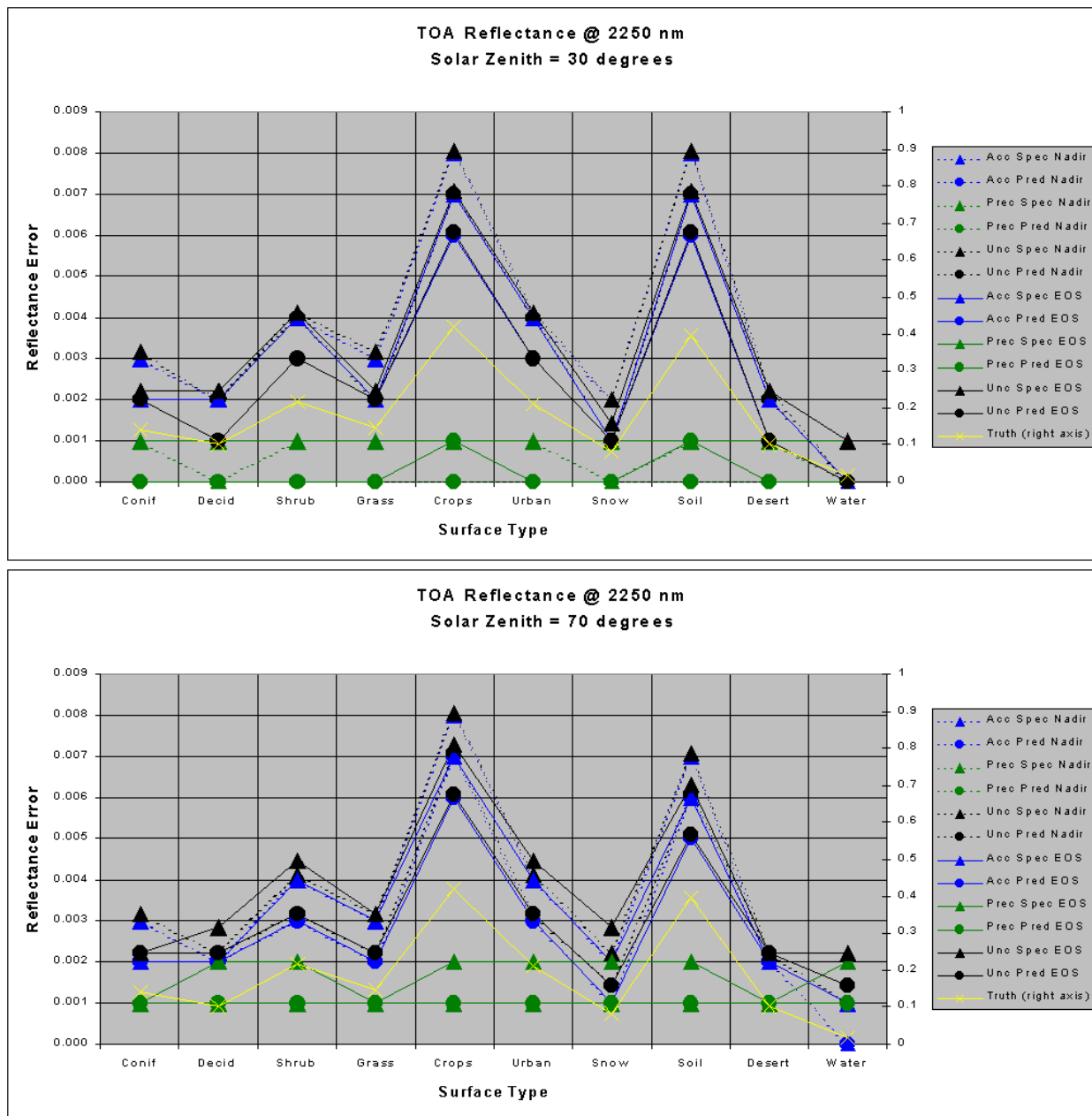


Figure 21. TOA reflectance errors at 2250 nm, for nadir and edge of scan, at solar zenith of 30 degrees (top) and 70 degrees (bottom), using both specified and predicted sensor performance as input.

3.4.3.6 Neural Network Intrinsic Errors

The neural network intrinsic error, which could also be called algorithmic or regression error, contains the effects of several items:

- 1) Atmospheric variability, including variations in aerosol type and optical thickness

- 2) Narrow to broadband conversion, including variations between surface types
- 3) Angular variability—variations in solar zenith, viewing zenith, and relative azimuth—including BRDF and atmospheric effects
- 4) Training error, or the inability of the network to achieve perfect performance within its training data set
- 5) Non-uniqueness, or the difficulty in completely decoupling atmospheric and surface effects when a TOA reflectance field has multiple possible surface solutions

Of these errors, the fifth could semantically be absorbed into the first three for simplicity, the route chosen here. Training error can be brought to a very low level by placing more stringent requirements on convergence or by adding connections and weights to the network. This must be balanced, however, against the tendency to overtrain the network, which renders it less robust when applied to non-training data. In general, the training error can be brought to below 0.01 albedo units globally, if sufficient training data are available at the outset. This last assumption is not trivial, and it will be addressed at length in Version 5 of this ATBD. For now, it is sufficient to note that the training strategy for SASA2 will begin with comprehensive radiative transfer simulations, and that these will be phased out in favor of real measurements from MODIS, and eventually from VIIRS.

The baseline for Surface Albedo at the end of Phase I was to employ SASA2 for all surfaces. Since that time, increased confidence from recent validation efforts for the MODIS approach has led to the adoption of SASA1 for dark surfaces. It was found late in Phase I that SASA2 could achieve the SRD uncertainty requirements for all surfaces, including snow, at moderate viewing angles. In Phase II, new simulations for snow at the edge of the VIIRS scan indicate that even under extreme geometry, SASA2 is fairly faithful to its training set, as shown in Table 7. The uncertainty specification is exceeded slightly, as the algorithm is primarily targeting the center of the range of true albedos; this can be mitigated in the future with different approaches to training, the results of which will be presented in a later version of this document. For example, more training data can be generated for the edge bins to reduce the dominance of the center bin. Again, these simulations do not include realistic simulations of surface BRDF, however the training set does include a range of aerosol optical thickness from 0.1 to 0.3, in addition to four separate aerosol types (urban, rural, desert, and maritime), with solar zenith ranging over ten degrees and view zenith also ranging over ten degrees (extending, in fact, to slightly beyond the actual limit of the VIIRS scan angle). Forward scattering from 0 out to 45 degrees in relative azimuth was also implemented here. The resulting test data set therefore includes quite a wide range of variation for a single neural network, despite the assumption of a Lambertian surface.

Table 7. Phase II results for SASA2 over snow, at the edge of the VIIRS scan.

Albedo Range	# Samples	Accuracy	Precision	Uncertainty
0.55-0.60	603	0.037	0.017	0.041
0.60-0.65	1175	0.001	0.018	0.018
0.65-0.70	870	0.035	0.016	0.038

Sensitivity studies that explicitly extract the contributions of atmospheric and conversion error to the neural network intrinsic error have not been conducted during Phase I. This will be a necessary task for completeness in Phase II. For the present, all of the neural network errors have been combined into a single term for the purposes of albedo error budgeting. The neural network error consumes virtually all of the precision error budget across the measurement range. Accuracy receives contributions from both calibration and neural network error, however the calibration errors can be largely mitigated by post-launch training, therefore the total accuracy error presented here is also almost entirely from neural network intrinsic error. As a consequence, the total uncertainty for SASA2 can be treated similarly—as a result primarily of neural network intrinsic error.

Late in Phase, I, the stick modeling data set presented in Section 3.4.3.5 was used to conduct an end-to-end, stratified performance summary for SASA2, for both dark and bright surface types. The results are shown in Figure 22 and Figure 23, for accuracy and uncertainty, respectively. Accuracy performance has little difficulty beating the threshold requirement. The fine HCS uncertainty requirement at nadir is also achievable for all surface types.

For an assessment of the overall performance of the MODIS approach, the reader is directed to Lucht *et al.* (2000). More details on the specific performance of the adapted SASA1 approach will be presented in a later version of this ATBD.

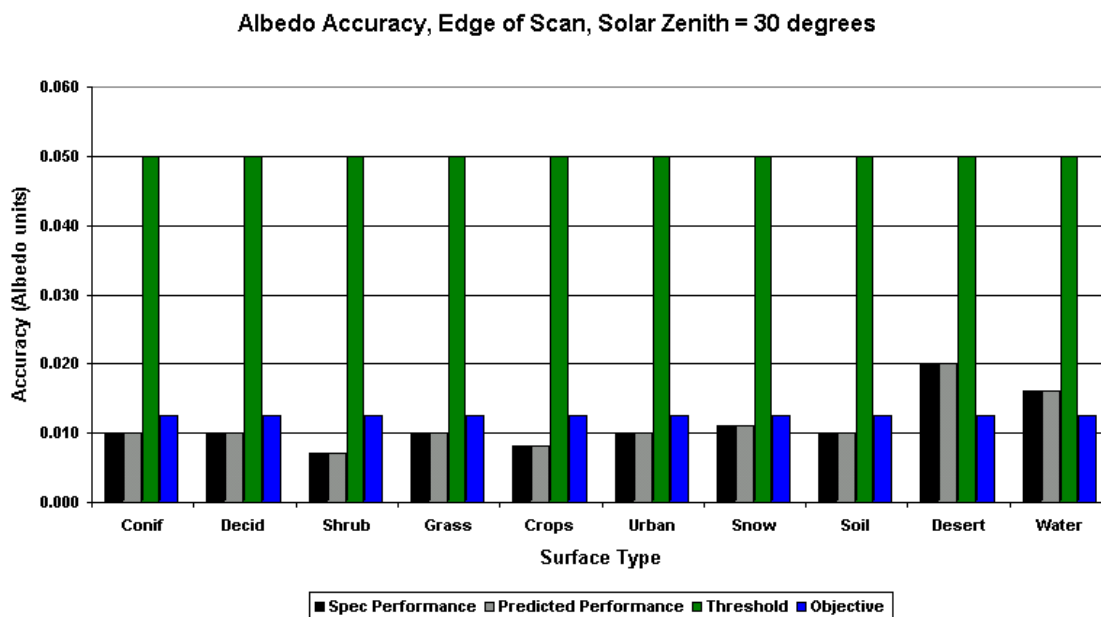


Figure 22. Albedo accuracy performance, spec and predicted, at edge of scan for a solar zenith of 30 degrees. Note negligible difference between spec and predicted sensor performance for calibration, assuming the algorithm is trained post-launch with real VIIRS data.

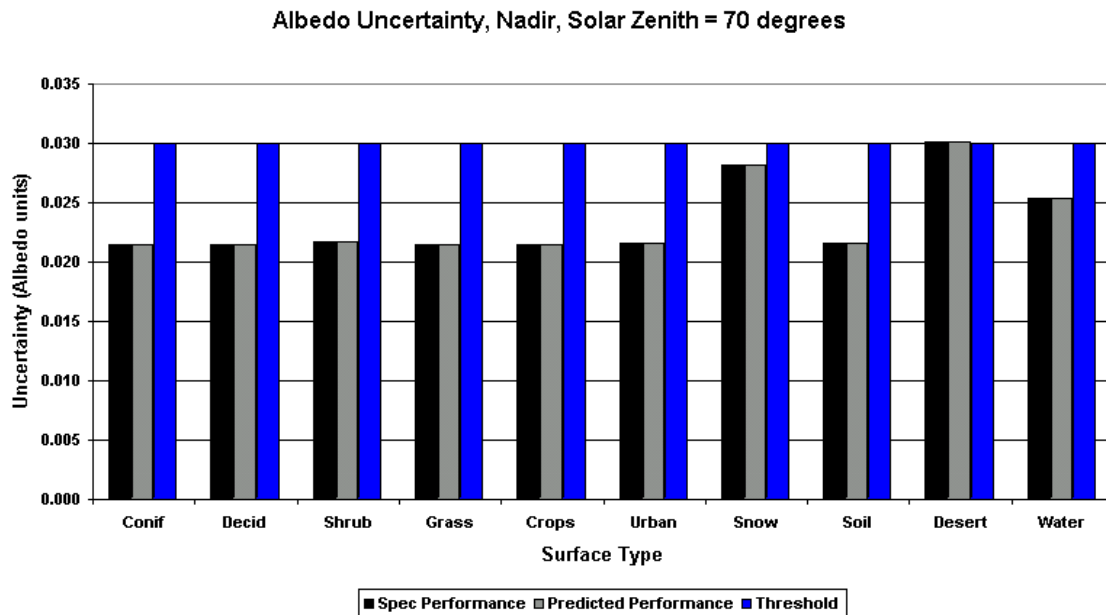


Figure 23. Albedo uncertainty performance, spec and predicted, at nadir for a solar zenith of 70 degrees. Nadir uncertainty requirement (fine product) is 0.03 threshold.

3.5. PRACTICAL CONSIDERATIONS

3.5.1. Numerical Computation Considerations

The VIIRS SRD (NPOESS IPO, 1998) states the following (Paragraph SRDV 3.2.1.5.4-1):

The scientific SDR and EDR algorithms delivered by the VIIRS contractor shall be convertible into operational code that is compatible with a 20 minute maximum processing time at either the DoD Centrals or DoD field terminals for the conversion of all pertinent RDRs into all required EDRs for the site or terminal, including those based wholly or in part on data from other sensor suites.

RDR here stands for Raw Data Record. This essentially means that any and all EDRs must be completely processed from VIIRS raw data, which include calibration and georeferencing information, within 20 minutes from the time the raw data are available. This requirement is a strong reminder that VIIRS is an operational instrument.

For SASA2, the challenges posed by the SRD time requirement are minimal. The neural network is merely a single equation at run time. Training is conducted offline. For SASA1, our approach shifts most of the computational burden offline as well; the inversion procedure takes place once per day to generate the Gridded Surface Albedo IP. All that is required in real-time is a simple interpolation routine to bring the black sky and white sky albedo to the pixel level, followed by the application of simple empirically based formulae. More detail on the computational load associated with these processes will be presented in Version 5 of this ATBD.

3.5.2. Programming and Procedural Considerations

Numerical computation load and complexity of operational code are typically rather well correlated. More intensive algorithms will generally be manifested in larger and more intricate source code. The code itself can have a significant impact on numerical computation load if it is not developed efficiently. The albedo algorithm is not expected to cause many problems in this regard. The simplicity of the real-time portion of SASA2 translates into only moderate amounts of code using basic mathematical routines. Storage of the network coefficients should not present a problem; the Phase I version contained approximately 100 per angular bin, and the addition of angles as inputs will less than double the total number of weights, plus there will only be a single network to handle all solar/viewing geometry. These numbers are small compared to the various lookup tables existing within the VIIRS system.

VIIRS Phase II efforts are largely software-focused, and the methodology for this development work is based on sound and proven principles, as discussed in the VIIRS Algorithm Software Development Plan [Y6635]. The present maturity of the VIIRS software is detailed in the VIIRS Algorithm Software Maturity Assessment document [Y6661]. The maturity and remaining Phase II tasks for the algorithms themselves is summarized in the VIIRS Algorithm/Data Processing Technical Report [Y7040]. The software designs relevant to Surface Albedo are summarized in the VIIRS Context Level Software Architecture [Y2469], Land Module Level Software Architecture [Y2474], Land Module Level Detailed Design [Y2483], and Surface Albedo IP Unit Level Detailed Design [Y2499]. These designs will be tested at the system level as described in the most recent versions of the VIIRS Software Integration and Test Plan [Y3236], Algorithm Verification and Validation Plan [Y3237], and System Verification and Validation Plan [Y3270]. A summary of the ultimate strategy for operational application of the system of VIIRS algorithms is provided in the VIIRS Operations Concept document [Y2468]. The VIIRS Interface Control Document (ICD [Y2470]) provides more detail on the specifics of ancillary data requirements for Surface Albedo and other VIIRS products.

3.5.3. Configuration of Retrievals

The primary adjustable parameters for the retrieval of the albedo product are those that govern the overall stratification with respect to the expected quality of the output. These parameters have been merged into the generalized Land Quality Flag (LQF) structure, which is appended to the output of the Surface Reflectance IP. For more detail on the LQF output, the reader is directed to [Y2411]. Specifics on its application to Surface Albedo will be provided in Version 5 of this ATBD.

3.5.4. Quality Assessment and Diagnostics

Again, the reader is directed to [Y2411] for a discussion of quality assessment regarding the LQF output. Some additional diagnostics will be required for SASA2, to ensure the neural network functions well over time. In fact, the network will provide an excellent means of monitoring the long-term stability of the sensor in the nine relevant bands listed in Table 2.

3.5.5. Exception Handling

The algorithm performance will be guaranteed to meet the system specifications [SS154650] only if the assumptions listed in Section 4.1 are valid and the limitations listed in Section 4.2 are not encountered. Missing data can be interpolated or assigned the most recently obtained value, however this is not currently planned for the VIIRS processing system. The LQF will specify whether a given pixel should be expected to meet the specifications for Surface Albedo.

3.6. VALIDATION

In order to evaluate the performance of the Surface Albedo algorithm, an initial Albedo Validation Plan (AVP) has been established. This AVP has been adopted from the MISR and MODIS validation program and will be refined in a future version of this ATBD. Also, the MODIS efforts for continued validation of SASA1's heritage will be of tremendous value in reducing VIIRS system-level risks. For any EDR, we define the following terms.

Definition: *Product validation* constitutes a comparison between:

- (a) geophysical products retrieved by applying VIIRS-EDR algorithms to surface or tropospheric-leaving radiances measured by a VIIRS simulator instrument, or top-of-atmosphere (TOA) radiances measured by VIIRS, with
- (b) geophysical products retrieved from downwelling sky and solar radiation measured at the surface, together with conventional retrieval algorithms based on such measurements. Analysis of systematic and random errors in each pathway (e.g., downward-looking and upward-looking) is included.

Definition: A *field experiment* is a comparison of two geophysical parameter retrievals based on independent measurements.

Definition: A *field campaign* is an activity that involves conducting one or more field experiments.

The AVP describes how, in the pre-launch period, an output is generated that accurately represents (in a scientific sense) what it claims. Secondly, the plan describes how each data product, in the post-launch period, can be shown to accurately represent the corresponding radiometric or environmental (“geophysical”) parameters. The plan contains the following elements:

- Description of validation objectives.
- Specification of VIIRS products that can be validated by simple ground-based or aircraft-based procedures.
- Specification of conventional methods for measuring each product from a ground perspective.
- Definition of algorithm development needs, beyond that existing and available.

- Definition of instrumentation needs, uses, calibration, and intercomparison procedures, including:
 - Ground-based for applicable atmosphere, surface, and TOA/cloud retrievals
 - Aircraft VIIRS simulator and supporting instruments (e.g., aircraft sunphotometry)
 - Aircraft measurements (e.g., in-situ aerosol sampling)
 - Spacecraft candidates with view capabilities that bear upon comparisons with VIIRS.
- Specification of test sites for both algorithm validation (pre-launch) and product verification (post-launch).
- Description of the nature of field experiments to achieve simultaneous ground-based and aircraft simulator (pre-launch) or VIIRS (post-launch) observations, including required experimental conditions, deployment of ground-based resources, aircraft flight line configurations, and timing of overpasses to simulate VIIRS observing conditions.
- Description of post-experiment data reduction and error analysis procedures.
- Plans for archival and publication of validation/verification results.

The AVP is designed to accomplish the following objectives in the pre-launch and post-launch time frames.

AVP pre-launch objectives:

- Validate SASA1 and SASA2 using simulated data
- Procure and adapt/modify essential field instruments for solar, sky and ground-reflected radiation measurements to implement retrieval algorithms
- Organize field campaigns at selected test sites, encompassing essential parts of the different surface conditions on global scale
- Demonstrate the ability to make field measurements of radiometric quantities
- Demonstrate the ability to derive both the spectral and the broadband albedo from ground measurements
- Specifically evaluate the sensitivity of VIIRS airborne simulator and field instruments to validate VIIRS EDR retrieval algorithms
- Develop new software to analyze data for VIIRS needs (e.g., software for PARABOLA or any other ground-based instrument-measured data)
- Cooperate and discuss with the calibration team the results of the measurements/ simulations/ calibrations found for the VIIRS simulator instruments as well as the VIIRS sensor.

AVP post-launch objectives:

- Validate SASA1 and SASA2 using satellite-derived data
- Continue to validate SASA1 and SASA2 as needed
- Discuss the measurements delivered by the VIIRS sensor with the calibration team
- Calibrate the VIIRS simulator instruments in constant time intervals to uncover instrument degradation and to keep track of possible changes in performance of the VIIRS sensor
- Conduct field experiments on the designated test sites coordinated with underflights of airborne instruments and a VIIRS overpass
- Compare/analyze of VIIRS-derived albedo and the albedo derived from other satellite systems.

Table 8, Table 9, and Table 10 list ground, airborne, and satellite instruments, respectively, which can provide comparison data in support of the AVP. Table 11 lists general testbed candidates.

The following guidelines have been applied for the selection of the NPOESS VIIRS test beds:

- Co-locate algorithm and product validation experiments (where possible) with other major surface and/or atmospheric experiments, to take advantage of resources and infrastructure present, and make the sharing of scientific data possible.
- Logistic convenience for surface and aircraft observations, to minimize field access problems, as well as aircraft flight hour costs. Sites may be occupied several times over a period of years. Sites in North America and the continental United States (plus adjacent ocean waters) have thus been favored whenever possible, except where significant advantages may be obtained by joining forces with other groups elsewhere.
- Availability of records of seasonal conditions to optimize chances for choices of clear sky opportunities for aerosol and surface reflectance studies.

Table 8. Ground based instruments for the AVP.

Instrument	Purpose
Cimel Sunphotometer	Spectral aerosol optical depth, aerosol scattering and absorption properties
GPS	Geolocation
MFRSR	Imaginary part of the aerosol refractive index and an average Lambertian surface reflectance
PARABOLA III	Bidirectional reflectance factor (BRF), albedo
Reagan sunphotometers	Spectral aerosol optical depth, ozone optical depth, column abundance of water
Weather station	Meteorology

Table 9. Airborne instruments for the AVP.

Instrument	Purpose
AirMISR	Multi-angle multi-spectral images
ASAS	Multi-angle multi-spectral images
AVIRIS	Nadir viewing multi-spectral images
ATS	Spectral atmospheric extinction
C-131 A	Meteorological, aerosol/cloud properties, radiometry
Camera (e.g., Nikon, FOV: 180°)	Cloud detection, imagery
GPS	Geolocation
MAS	Multi-angle multi-spectral images (MODIS)
RC-10	Aerial photographs

Table 10. Satellite measurements to compare with VIIRS for the AVP.

Instrument	Purpose
LANDSAT	Intercomparison with VIIRS albedo
AVHRR	Intercomparison with VIIRS albedo
MODIS	Intercomparison with VIIRS albedo

Table 11. Possible testbeds for the AVP.

Instrument	Purpose
AERONET	Aerosol Network (World)
ARM CART	Atmospheric Radiation Measurement, Cloud and Radiation Test Bed (Lament, OK)
ACE II	Aerosol Characterization Experiment (North Atlantic Region)
BOREAS	Boreal Ecosystem-Atmosphere Study (Canada)
EOPACE	Electro-optic Propagation Assessment in Coastal Environment (South/Central Calif.)
HAPEX-Sahel, FIFE, TRACE-A, SAFARI, LBA	Atm. Parameters over land cover gradients
ISIS	NOAA Integrated Surface Irradiance Study (US)
OTTER, SCAR-A/C, GLCTS	Land Cover, BRDF /Albedo, VI
SCAR-B	Smoke, Clouds, and Radiation (Brazil)
TARFOX	Tropospheric Aerosol Radiative Forcing Observational Experiment (Coastal Eastern US in summer)
White Sands/Railroad Playa	Instrument calibration

4.0 ASSUMPTIONS AND LIMITATIONS

4.1 ASSUMPTIONS

The following assumptions apply to the albedo retrieval algorithms described in this document:

1. Specifications on sensor performance as described in [PS154650].
2. The existence of an at-launch database for generating the Gridded Surface Albedo IP and the Gridded Daily Surface Reflectance IP, until these VIIRS products have phased completely in.
3. National and international validation networks that can be tapped for the testing of both SASA1 and SASA2 before the launch of NPP, and again before the first launch of NPOESS.

4.2 LIMITATIONS

The following limitations apply to the albedo retrieval algorithm described in this document:

1. The assumption of a plan-parallel scattering medium must be valid for SASA2. Thus, the solar and observer zenith angles are constrained to values less than 70° for specification quality (retrievals conducted out to 85°). Similar angular limits apply to SASA1.
2. Ocean retrievals will not be performed in areas of 30° (value to be reviewed) around sun glint.
3. Retrievals will be questionable in regions with very heavy aerosol loading, such as associated with local volcanic eruptions, fires, or sandstorms.

5.0 REFERENCES

- Andrieu, B., F. Baret, S. Jacquemoud, T. Malthus, and M. Steven (1997). Evaluation of an Improved Version of SAIL Model for Simulating Bidirectional Reflectance of Sugar Beet Canopies. *Rem. Sens. Env.*, 60:247-257.
- Baret, F. and G. Guyot (1991). Potentials and Limits of Vegetation Indices for LAI and APAR Assessment. *Rem. Sens. Env.*, 35:161-173.
- Bicheron, P., and M. Leroy (2000). Bidirectional reflectance distribution function signatures of major biomes observed from space. *J. Geophys. Res.*, D105, 26669-26681.
- Blanchet, J. and R. List (1983). Estimation of optical properties of arctic haze using a numerical model. *Atmos.-Ocean*, 21, 444-465.
- Charney, J., W.J. Quirk, S. Chow, and J. Kornfield (1977). A comparative study of the effects of albedo change on droughts in Semi-arid regions, *J. Atmos. Sci.*, 34, 1366.
- Chase, T.N. *et al.* (1996). Sensitivity of a GCM to global changes in LAI. *J. Geophys. Research-Atmospheres*, 101 (D3), 7393-7408.
- Culf, A.D., *et al.* (1995). The albedo of Amazonian forest and ranchland. *J. Climate*, 8 (6), 1544-54.
- Deering, D.W. and P. Leone (1986). A sphere-scanning radiometer for rapid directional measurements of sky and ground radiance. *Rem. Sens. Environm.*, 19:1-24.
- d'Entremont, R. E., C. L. Barker Schaaf, W. Lucht, and A. H. Strahler (1999). Retrieval of red spectral albedo and bidirectional reflectance using AVHRR HRPT and GOES satellite observations of the New England region, *J. Geophys. Res.*, D-104, 6229-6239.
- Dickinson, R.E. (1983). Land surface processes and climate-surface albedos and energy. *Adv. Geophys.*, 25:305-353.
- Dickinson, R.E. (1995). Land processes in climate models, *Remote Sens. Environ.*, 51, 27--38.
- Diner, D.J., *et al.* (1989). MISR: A Multiangle Imaging Spectroradiometer for Geophysical and Climatological Research on EOS. *IEEE Trans. Geos. R. Sens.*, 27:200-214.
- Diner, D.J. *et al.* (1996). Multiangle Imaging Spectroradiometer (MISR) Level 2 Surface Retrieval. <http://eosps0.gsfc.nasa.gov/atbd/misrtables.html>. (ATBD-MISR-10).
- Engelsen, O., B. Pinty, M.M. Verstraete, and J.V. Martonchik (1996). Parametric bi-directional reflectance factor models: evaluation, improvements and applications. ECSC-EC-EAEC Brussels Luxembourg Catalogue: CL-NA-16426-EN-C, European Commission, JRC, IRSA, Ispra, Italy, 1996. European Commission, Directorate General XII, L-2920 Luxembourg.

- Garrat, J.R. (1993). Sensitivity of climate simulations to land surface and atmospheric boundary layer treatments – a review. *J. Climate*, 6, 419-449.
- Gobron, N., B. Pinty, M.M. Verstraete, and Y. Govaerts (1997). A semidiscrete model for the scattering of light by vegetation. *J. Geophys. Res.*, 102, NO. D8, pages 9431-9446.
- Gordon, H.R. *et al.* (1983). Phytoplankton pigment concentration in the Middle Atlantic Bight: Comparison of ship determinations and Coastal Zone Color Scanner measurements. *Appl. Opt.*, 22, pp. 3929.
- Graedel, T.E. and P.J. Crutzen (1994). *Chemie der Atmosphäre*, Spektrum Akademischer Verlag GmbH, Heidelberg, Berlin, Oxford, ISBN 3-86025-204-6.
- Guenther, B. (1997). Moderate Resolution Imaging Spectroradiometer (MODIS) Calibration Plan. <http://eospsso.gsfc.nasa.gov/atbd/modistables.html>. (ATBD-MODIS-01).
- Han, W. (1996). Remote Sensing of Surface Albedo and Cloud Properties in the Arctic from AVHRR Measurements, Ph.D. Thesis, Geophysical Institute, University of Alaska, Fairbanks, Alaska 99775.
- Hansen, J.E., G. Russell, D. Rind, P. Stone, A. Lacis, L. Travis, S. Lebedeff, and R. Ruedy, 1983: Efficient three-dimensional global models for climate studies: Models I and II. *Mon. Wea. Rev.*, 111, 609-662.
- Hautecoeur, O., and M. M. Leroy (1998). Surface bi-directional reflectance distribution function observed at global scale by POLDER/ADEOS, *Geophys. Res. Letters*, 22, 4197-4200.
- Henderson-Sellers, A. and Pitman, A.J. (1992). Land-surface schemes for future climate models: Specification, aggregation, and heterogeneity. *J. Geophys. Res.*, 97:2687-2696.
- Henderson-Sellers, A., Z.-L. Zhang, and R. E. Dickinson (1993). The project for intercomparison of land-surface parameterization schemes, *Bull. Am. Meteorol. Soc.*, 74, 1335-1349.
- Hook, S.J. (1998). Advanced Spaceborne Thermal Emission and Reflection Radiometer (ASTER) Spectral Library. <http://speclib.jpl.nasa.gov/>.
- Hucks, J.C. (1998). VIIRS Testbed Sensor Modeling Efforts, Phase I. Raytheon Systems Company Internal Memorandum Y1629.
- Iaquinta, J., and B. Pinty (1995). Adaption of a Bidirectional Reflectance Model including the Hot-Spot to an optically thin canopy, Proceedings of the 6th International Colloquium-Physical Measurements and Signatures in Remote Sensing, Val d'Isere, France, January 17-21, pages 683-690.
- Irons, J. *et al.* (1992). Prediction and Measurement of Soil Bidirectional Reflectance. *IEEE Trans. Geos. R. Sens.*, 30, No. 2.
- Jacquemoud, S. and F. Baret (1990). PROSPECT: A model of Leaf Optional Properties Spectra. *Rem. Sens. Environ.* 34: 75-91.

- Johansson, E.M., F.U.Dowla, and D.M.Goodman (1992). Backpropagation learning for multiplayer feed-forward neural networks using the conjugate gradient method. *International Journal of Remote Sensing*, 13, 2059-2068.
- Jupp, D.L.B., and A.H. Strahler (1991). A hotspot model for leaf canopies. *Rem. Sens. Env.*, 38:193-210.
- Justice, C. O., E. Vermote, J. R. G. Townshend, R. DeFries, D. P. Roy, D. K. Hall, V. V. Salomonson, J. L. Privette, G. Riggs, A. Strahler, W. Lucht, R. B. Myneni, Y. Knjazikhin, S. W. Running, R. R. Nemani, Z. Wan, A. R. Huete, W. vanLeeuwen, R. E. Wolfe, L. Giglio, J.-P. Muller, P. Lewis, and M. J. Barnsley (1998). The Moderate Resolution Imaging Spectroradiometer (MODIS): Land remote sensing for global change research, *IEEE Trans. Geosci. Remote Sens.*, 36, 1228-1249.
- Kimes, D.S., and P.J. Sellers (1985). Inferring hemispherical reflectance of the Earth's surface for global energy budgets from remotely sensed nadir or directional radiance values. *Rem. Sens. Environ.*, 18, pp 205.
- King, M. D., Y. J. Kaufman, W.P. Menzel, and D. Tanre (1992). Remote sensing of cloud, aerosol and water vapor properties from the MODerate Imaging Spectroradiometer (MODIS), *IEEE Trans. Geosci. Remote Sens.*, 30, 2-27.
- Larsen, N. Personal communication, August 1997.
- Lean, J., and P.R. Rowntree (1993). A GCM simulation of the impact of Amazonia deforestation on climate using an improved canopy representation. *Quart. J. Roy. Meteor. Soc.*, 119, 509-530.
- Lee, T.Y., and Y.J. Kaufman (1986). Non-Lambertian Effects on Remote Sensing of Surface Reflectance and Vegetation Index. *IEEE Trans. Geosci. Rem. Sens.*, GE-24, 699-708.
- Leroy, M., J. L. Deuze, F. M. Breon, O. Hautecoeur, M. Herman, J. C. Buriez, D. Tanre, S. Bouffies, P. Chazette, and J.-L. Roujean (1997). Retrieval of atmospheric properties and surface bidirectional reflectances over land from POLDER/ADEOS, *J. Geophys. Res.*, 102, 17023-17037.
- Lewis, P., and M. J. Barnsley (1994). Influence of the sky radiance distribution on various formulations of the earth surface albedo, Proc. Conf. Phys. Meas. Sign. Remote Sens., Val d'Isere, France, 707-715.
- Li, X., and A. H. Strahler (1992). Geometric-optical bi-directional reflectance modeling of the discrete crown vegetation canopy: Effect of crown shape and mutual shadowing, *IEEE Trans. Geosci. Remote Sens.*, 30, 276-292.
- Li, Z., J. Cihlar, C. Zheng, L. Moreau, and H. Ly (1996). The bidirectional effects of AVHRR measurements over boreal regions, *IEEE Trans. Geoscience. Remote Sens.*, 34, 1308-1322.
- Liang, S., and A.H. Strahler (1993). Calculation of the Angular Radiance Distribution for a Coupled Atmosphere and Canopy. *IEEE Trans. Geosci. Rem. Sens.*, GE-31, 491-502.

- Liang, S., A.H. Strahler, and C. Walthall (1999). Retrieval of land surface albedo from satellite observations: a simulation study. *Journal of Applied Meteorology*, 38, 712-725.
- Lofgren, B. M. (1995). Surface albedo-climate feedback simulated using two-way coupling, *J. Climate*, 8, 2543-2562.
- Lucht, W. (1998). Expected retrieval accuracies of bi-directional reflectance and albedo from EOS-MODIS and MISR angular sampling, *J. Geophys. Res.*, 103, 8763-8778.
- Lucht, W., C.B. Schaaf, and A.H. Strahler (2000). An Algorithm for the retrieval of albedo from space using semiempirical BRDF models, *IEEE Trans. Geosci., Remote Sens.*, 38, 977-998.
- Lucht, W., and P. Lewis (2000). Theoretical noise sensitivity of BRDF and albedo retrieval from the EOS-MODIS and MISR sensors with respect to angular sampling, *Int. J. Remote Sensing*, 21, 81-98.
- Martonchik, J.V., and D.J. Diner (1992). Retrieval of aerosol optical properties from multi-angle satellite imagery. *IEEE Trans. Geosci. Rem. Sens.*, GE-30, pp. 223.
- Martonchik, J. V., D. J. Diner, B. Pinty, M. M. Verstraete, R. B. Myneni, Y. Knjazikhin, and H. R. Gordon (1998). Determination of land and ocean reflective, radiative, and biophysical properties using multiangle imaging, *IEEE Trans. Geosci. Remote Sens.*, 36, 1266-1281.
- Masters, T. (1993). *Practical neural network recipes in C++*. Academic Press, 493 pp.
- Matthews, E. (1983). Global vegetation and land use: New high resolution data bases for climate studies. *J. Clim. Appl. Meteorol.*, 22:474-487.
- Miller, S. (1998). Guidance for Band Response, Calibration Issues, Internal Memorandum, Ref: 98VIIRSL00017, July 30.
- Mintz, Y. (1984). The sensitivity of numerically simulated climates to land-surface conditions, *The Global Climate*, edited by J. Houghton, pp. 79-105, Cambridge University Press, New York.
- Myneni, R.B. *et al.* (1995). Optical Remote Sensing of Vegetation: Modeling, Caveats, and Algorithms. *Rem. Sens. Env.*, 51:169-188.
- Myneni, R.B., R. Nemani and S. Running (1997). Estimation of Global Leaf Area Index and Absorbed PAR Using Radiative Transfer Models. *IEEE Transactions on Geoscience and Remote Sensing*, Vol. 35, No. 6.
- Nemani, R.R. *et al.* (1996). Global vegetation cover changes from coarse resolution satellite data. *J. Geophys. Research-Atmospheres*, 101 (D3), 7157-7162.
- Nicodemus, F.E., J.C. Richmond, J.J. Hsia, I.W. Ginsberg, and T. Limperis (1977). Geometrical Considerations and Nomenclature for Reflectance., Technical report, National Bureau of Standards, NBS Monograph 160, Dept. of Commerce, Washington, D.C.

- Nilson, T., and A. Kuusk (1989). A Reflectance Model for the Homogeneous Plant Canopy and Its Inversion. *Rem. Sens. Env.*, 27:157-167.
- Ni, W. and S. Miller (2000), NPOESS/VIIRS Surface Reflectance ATBD, Version 3.0. Document # Y2411.
- NPOESS IPO (1998). Visible/Infrared Imager/Radiometer Suite (VIIRS) Sensor Requirements Document (SRD). Prepared by Associate Directorate for Acquisition, NPOESS Integrated Program Office, Revision 1.
- Pinty, B., and M.M. Verstraete (1991). Extracting information on surface properties from bidirectional reflectance measurements. *J. Geophys. Res.*, 96, pp. 2865.
- Pinty B., F. Roveda, M. M. Verstraete, N. Gobron, Y. Govaerts, J. V. Martonchik, D. J. Diner, and R. A. Kahn (2000a). Surface Albedo Retrieval from METEOSAT Part 1 : Theory, *J. Geophys. Res.*, D-105, 18099-18112.
- Pinty B., F. Roveda, M. M. Verstraete, N. Gobron, Y. Govaerts, J. V. Martonchik, D. J. Diner, and R. A. Kahn (2000b). Surface Albedo Retrieval from METEOSAT Part 2 : Applications, *J. Geophys. Res.*, D-105, 18113-18134.
- Privette, J., T. Eck, and D.D. Deering (1997). Estimating spectral albedo and nadir reflectance through inversion of simple BRDF models with AVHRR/MODIS-like data. *J. Geophys. Res.*, D102, 29529-29542.
- Qi, J., M.S. Moran, F. Cabot, and G. Dedieu (1995). Normalization of Sun/View Angle Effects Using Spectral Albedo-Based Vegetation Indices. *Rem. Sens. Env.*, 52:207-217.
- Rahman, H., B. Pinty, and M. M. Verstraete (1993). Coupled surface-atmosphere reflectance (CSAR) model, 2, Semiempirical surface model usable with NOAA advanced very high resolution radiometer data, *J. Geophys. Res.*, 98, 20791-20801.
- Ross, J. K. (1981). The Radiation Regime and Architecture of Plant Stands, Dr. W. Junk, Norwell, Mass., 392 pp.
- Ross, J., and A. Marshak (1989). The Influence of Leaf Orientation and the Specular Component of Leaf Reflectance on the Canopy Bidirectional Reflectance. *Rem. Sens. Env.*, 27:251-260.
- Roujean, J.-L. M. Leroy, and P. Y. Deschamps (1992). A bi-directional reflectance model of the Earth's surface for the correction of remote sensing data, *J. Geophys. Res.*, 97, 20455-20468.
- Rumelhart, D.E., G.E. Hinton, and R.J. Williams (1986). Learning internal representations by error propagation. In *Parallel distributed processing: explorations in the microstructure of cognition, vol. 1: foundations*, eds. D.E. Rumelhart and J.L. McClelland. MIT Press. 547 pp.

- Running, S. (1990). Estimating terrestrial primary productivity by combining remote sensing and ecosystem simulation, *Remote sensing of Biosphere Functioning*, edited by R. Hobbs and H. Mooney (New York: Springer-Verlag), pp.65-86.
- Running, S., *et al.* (1994). Terrestrial remote sensing science and algorithms planned for EOS/MODIS. *Int. J. Remo. Sens.*, Vol. 15, No. 17, 3587-3620.
- Running, S., R. Myneni, R. Nemani, and Joseph Glassy (1996). MODIS LAI (Leaf Area Index) and MODIS FPAR (Fraction Of Absorbed Photosynthetically Active Radiation), <http://eosps0.gsfc.nasa.gov/atbd/modistables.html> (ATBD-MOD-15).
- Saunders, *et al.* (1990). The determination of broadband surface albedo from AVHRR visible and near-infrared radiances. *Int. J. Remote Sensing*, 11(1): 49-67.
- Schaaf, C.B., and A.H. Strahler (1993). Solar Zenith Angle Effects on Forest Canopy Hemispherical Reflectances Calculated with a Geometric-Optical Bidirectional Reflectance Model. *IEEE Trans. Geosci. Rem. Sens.*, GE-31, 921-927.
- Schaaf, C. B., F. Gao, A.H Strahler, W. Lucht, X. Li, T. Tsang, N. Strugnell, X. Zhang, Y. Jin, J.-P. Muller, P. Lewis, M. Barnsley, P. Hobson, M. Disney, G. Roberts, M. Dunderdale, C. Doll, R. d'Entremont, B. Hu, S. Liang, and J. Privette (2001). First Operational BRDF, Albedo, and Nadir Reflectance Products from MODIS, submitted *Remote Sensing Environ.*
- Sellers, P.J., *et al.* (1994). A global 1 by 1 NDVI data set for climate studies. Part 2: The generation of global fields of terrestrial biophysical parameters from the NDVI. *Int. J. Rem. Sens.*, 15 (17), 3319-46.
- Sellers, P.J., *et al.* (1996). A Revised Land Surface Parameterization (SiB2) for Atmospheric GCMs. Part I: Model Formulation. *J. Climate*, 9:676-705.
- Strugnell, N., W. Lucht and C. Schaaf (2001). A global albedo data set derived from AVHRR data for use in climate simulations, *Geophys. Res. Let.*, 28, 191-194.
- Strugnell, N., and W. Lucht (2001). Continental-scale albedo inferred from AVHRR data, land cover class and field observations of typical BRDFs, *J. Climate*, 14, 1360-1376.
- Vermote, E., and A. Vermeulen (1999). MODIS Spectral Reflectances ATBD (ATBD-MOD-09), <http://eosps0.gsfc.nasa.gov/atbd/modistables.html>.
- Vogt, P. (1997). Retrieval of the LAI and the FAPAR from bidirectional reflectance factors at the top of the canopy (in German), Ph.D.-thesis, ISSN 0939-2963, ISRN DLR-FB--97-25.
- Vogt, P. (1998). Preliminary results for the albedo retrieval. Internal Memorandum Ref: 98VIIRSL00012, May 15, 1998.
- Vogt, P., M.M. Verstraete, B. Pinty, M. Menenti, A. Caramagno, M. Rast (1999). *On the retrieval accuracy of the albedo and BRDF fields: potential of the LSPIM/PRISM sensor.*

Report EUR 19016 EN, Space Applications Institute, Joint Research Centre, European Commission. 53 pp.

Wanner, W., X. Li, and A. H. Strahler (1995). On the derivation of kernels for kernel-driven models of bidirectional reflectance, *J. Geophys. Res.*, 100, 21077-21090.

Wanner, W., A. H. Strahler, B. Hu, P. Lewis, J.-P. Muller, X. Li, C. L. Barker Schaaf, and M. J. Barnsley (1997). Global retrieval of bidirectional reflectance and albedo over land from EOS MODIS and MISR data: theory and algorithm, *J. Geophys. Res.*, 102, 17143-17162.

Wilson, M.F., and A. Henderson-Sellers (1985). A Global Archive of Land Cover and Soil Data for Use in General Circulation Models. *J. Climatology*, 5, 119-143.